Restructuring of rotating spokes in response to changes in the radial electric field and the neutral pressure of a cylindrical magnetron plasma

M.Sengupta,[1, a)] A. Smolyakov,[1] and Y. Raitses[2]
[1)] *Department of Physics and Engineering Physics, University of Saskatchewan, Saskatoon, S7N5E2 Canada*
[2)] *Princeton Plasma Physics Laboratory, Princeton, New Jersey 08543, USA*

(Dated: 18 May 2021)

Nonlinear plasma structures in the partially magnetized ExB plasma of a cylindrical magnetron are investigated using 2D3V particle-in-cell Monte-Carlo collision simulations. In early phase of the discharge, plasma gradients and radial electric fields excite a lower hybrid type instability that forms long wavelength rotating density spokes. As the discharge grows in density by ionization and the cathode gets shielded by the formation of an ion-sheath, radial electric fields diminish in the quasineutral region of the discharge. This induces a transition of the spokes into short scale spoke-on-spoke modes. The short wavelength structures can be reversed back into a long spiral spoke by lowering the neutral pressure which revives the radial electric fields via a turbulent plasma expansion. Plasma phenomena connected to the rotating spoke include the anomalous radial transport and loss of electrons through the spoke, azimuthal dragging of ions by the spoke's field, plasma temperature modulations by the spoke structure, and formation of electron vortices around equipotential islands, in some cases with opposing rotations to the underlying ExB drift. Electron scattering from non-ionizing collisions with neutrals also have minor influence on the instability.

Keywords: partially magnetized ExB plasma, cylindrical magnetron, 2D3V PIC-MCC device simulation, macroscopic lower hybrid instability, Rotating spokes, mode transitions, radial electric field, density gradients, ionization, neutral pressure, elastic electron scattering

I. INTRODUCTION

Many low energy plasma applications such as electric space propulsion devices[1–3], ion sources used in material processing[4,5] etc., operate on a partially magnetized ExB plasma. In this configuration magnetized electrons ExB drift under crossed electric and magnetic fields, and unmagnetized heavier ions are transported along the electric field.

While the set-up is widely used for the extraction and propulsion of the heavier plasma component, it has the free energy of differential flow between the electrons and ions that can lead to disruptive instabilities associated with the ExB drift and density gradients[6] causing anomalous transport of magnetized electrons and collisionless plasma heating. One of the mechanism of the instabilities is kinetic[1,7,88–10] and could be described as a variety of the Buneman two-stream instability[11,12] leading to short length scale cross-field modes $\sim 1\,mm$[13–19]. Allowed to evolve, these modes will nonlinearly merge in an inverse cascade to form longer rotating structures with close resemblance to a nonlinear cross-field ion sound wave[9,12,20–26]. Such modes can emerge in homogeneous plasmas provided the ions remain unmagnetized, and a large perpendicular electric field (at least $\sim 10^4\,V/m$) omnipresent[12,22,26].

Another instability mechanism is related to the presence of the density gradients and can be traced back to basic Simon-Hoh instability[27–29] modified by a variety of effects such as electron inertia, collisions, and ionization. Electron inertia leads to the lower-hydrid modes and instability cut-off for shorter wavelengths, and collisions can be a source of weaker dissipative modes but also somewhat reduce the growth rate of the density gradient driven modes.

It should be noted that at this time there are no well defined parametric boundaries for the two mechanisms and it is expected that to some degree there could be mutual interactions between these mechanism in partially magnetized ExB devices. Based on current understanding, one would expect the kinetic destabilization is prevailing for the regimes with strong ExB electric field[30] while the density gradients drive instabilities are operating in the region of the lower electric field[31] (e.g. near-anode region of Hall thruster[32]). The spoke formation is thought to be related to the latter mechanisms involving density gradients and perhaps ionization.

The rotating spoke is an umbrella term that covers a range of long wavelength (a few mm to a few cm long) cross-field structures in partially magnetized ExB plasmas[33]. It seems that spokes emergence is affected by a variety of mechanisms. Plasma ionization at the energetic front of an azimuthal structure can create localized pressure gradients that not only propel the structure azimuthally but also act as positive feedback for the structure to grow into a rotating spoke[34–44]. The nonlinear inverse cascade from unstable small scale modes can

[a)] Corresponding Author; Electronic mail: mes707@mail.usask.ca, msengupta87@gmail.com

result in long wavelength ion-sound like rotating spokes structures[12,26]. Again, plasma density gradients aligned with the electric field can trigger a collisionless lower hybrid instability which excites rotating spokes emanating from the density gradient regions[29,33,45–48]. This last type of the instability in presence of ionization is the subject of this paper.

The focus of our study is on the transitions of lower hybrid modes[49,50] and associated nonlinear dynamics, transport and collisionless heating in presence of the ionization. It is discovered that the spoke in the cylindrical magnetron transit towards shorter wavelength due to the reduction of the radial electric field in the quasi-neutral region. When radial field is enhanced, e.g. by cloud expansion, the mode evolves to longer wavelengths. In the conditions of our numerical experiment the evolution of the radial electric field is controlled by the development of a cathode ion sheath. Additional control is provided by an applied change of the background neutral density.

The 2D3V Particle-In-Cell Monte Carlo collision (PIC-MCC) code PEC2PIC, which was recently used to investigate Electron Drift Instability (EDI) mode transitions in Hall thruster[26] and various other device simulations in the past (see Sec II), is now used for studying transitions of the lower hybrid rotating spoke in a cylindrical magnetron. The simulation model self-consistently develops an argon discharge initiated and maintained by pulsed radial injection of electrons from an inner cylindrical cathode into a homogeneous neutral background.

The nascent discharge is sparse and without a cathode sheath. Hence large radial electric fields well penetrate into the plasma exciting a macroscopic lower hybrid instability that manifests as a long wavelength rotating spoke. As the ion sheath forms, its shielding cuts off the electric field reaching the spoke, resulting in the spoke's breaking to form short spoke-on-spoke structures. As ionization increases plasma density further, the larger scale spoke collapses, leaving the short length scale structures. At this stage, reverse transitions are induced by a reduction of the neutral pressure. The plasma responds to the fuel depletion with a turbulent radial expansion that diffuses away the short structures, replacing them with a nonlinear long spiral spoke, made possible by resurgent radial electric fields.

The spoke's evolution is accompanied by interesting nonlinear dynamics such as anomalous radial transport and loss of electrons through the spoke, azimuthal dragging of ions by the spoke field, formation of small length electron vortices and plasma temperature profiles getting relatively cooler/hotter when the excited mode has a short/long length scale.

By conducting the experiment once with, and and once without non-ionizing electron-neutral collisions we found that Elastic Electron Scattering (EES) only add minor dissipative and diffusive effects to the mode dynamics.

Another interesting finding was that in spite of inherent inhomogeneity in the plasma fields and density profiles, a linear excitation of a distinct single azimuthal mode happened macroscopically on the profile. In the Appendix we discuss the insights provided by the linear local analytical model on the excitation of such a mode.

Sec II is outlines the PEC2PIC code, its benchmarks, and the numerical set-up of the present experiment. Sec III investigates the evolution of the spoke at a fixed neutral pressure without EES. Sec IV is a continuation of the Sec III experiment under an applied reduction of neutral pressure. In Sec V the Sec III simulation is repeated with the addition of EES to the model. Sec VI has convergence tests for the fidelity of the PIC simulation. Conclusions and discussions form Sec VII, followed by Acknowledgments, and then an Appendix on the macroscopic manifestation of the lower hybrid instability.

II. THE NUMERICAL SETUP

Three aspects of the numerical setup are elaborated in the following subsections: a) The numerical model for simulating a cylindrical magnetron configuration. b) The PIC-MCC code; past experiments, benchmarks, and convergence tests performed with the code. c) Technical justification for the values of mesh resolution, progression time step, super particle weight etc., used in the experiment.

A. Device model

The cross-section of a cylindrical dc magnetron[35,51,52] is simulated. Fig. 1a is a schematic cartoon of the set-up. The cathode is an inner cylinder of a radius 0.3 cm that is maintained at -200 Volts. A concentric outer cylindrical shell of radius 1.5 cm is the grounded anode. The cathode is electron emitting and both cylindrical walls are lossy and perfectly conducting. A uniform distribution of argon neutrals at a density of $1.2875 \times 10^{21}\, m^{-3}$ is maintained in the annular space all through the experiment. This density implies a background neutral pressure of 40 mTorr in the chamber at room temperature, 300 K. A uniform axial (into the plane in Fig. 1a) magnetic field of 0.015 Tesla is applied in the annular space.

A pulsed electron emission is used as it is computationally cheaper than simulating a continuous stream. Its implementation is further simplified by synchronizing the time-steps for the two population altering processes of electron emission and impact ionization.

To simulate a pulsed electron emission from the cathode, the macro-particle equivalent of 2.724×10^8 new electrons are introduced every 4^{th} simulation time-step (same as the MCC collision interval), where time-step $\delta t = 5\, ps$. The new electrons are arranged with randomly assigned azimuthal positions on a radial surface, r = 0.42 cm just outside the cathode. The injected electrons each carry an initial velocity of $2.3 \times 10^6\, m/s$ i.e. 15.69 eV, directed radially outwards. Injecting the electrons with equal energies instead of a distribution is a simplification of the

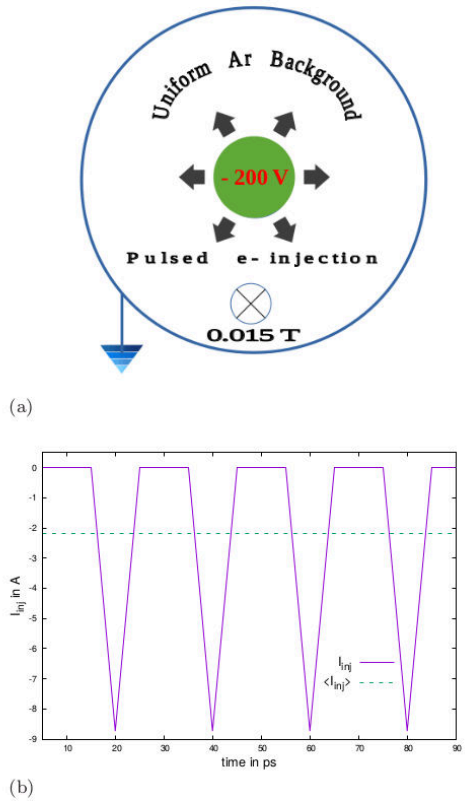

FIG. 1: Set-up for the numerical experiment: (a) A not-to-scale, schematic cartoon of the cylindrical magnetron cross-section. The inner cathode (green) has a radius of 0.3 cm and the outer grounded hollow anode (blue) is of radius 1.5 cm. (b) Graphical representation of the pulsed electron injection. I_{inj} is the injected radial electron current and $< I_{inj} >$ is it's pulse average.

model that assumes that these electrons and their secondaries are thermalized through ionizing collisions with the neutral background and collisionless heating mechanisms in the plasma. The $15.69\,eV$ value of the injection energy of the electrons is chosen so that they carry the minimum energy to start ionizing the argon background ($15.76\,eV$).

The resultant injection current is shown in Fig. 1b. The pulse period is $4\delta t$ with an injection phase of $1\delta t$ and a rest phase of $3\delta t$. In the injection phase the introduction of $N_{inj} = 2.724 \times 10^8$ electrons of charge e in one δt produces a local radial current , $I_{inj} = eN_{inj}/\delta t = -8.728\,A$ on the injection surface r = 0.42 cm. The average current of injection in the pulse period $4\delta t$ is $< I_{inj} >= 0.25\,I_{inj} = 2.182\,A$.

In this system there is no external feedback from the particle losses on the applied voltage, or on the electron injection rate, or even the argon gas density in the chamber. The three latter parameters are fixed in the experiment.

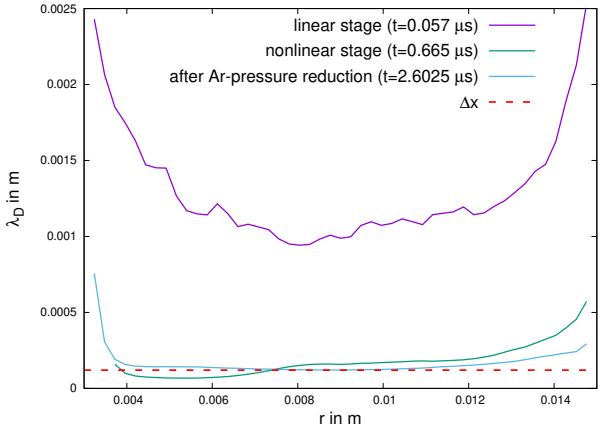

FIG. 2: Resolution of local Debye length, λ_D on grid in different stages of the instability. Here $\Delta x = 0.12\,mm$

B. PIC-MCC code

The Particle-in-cell simulation code used is **PEC2PIC** which stands for **P**arallelized **E**lectrostatic **C**artesian **2**D **P**article-**I**n-**C**ell code. Developers are M. Sengupta and R. Ganesh. PEC2PIC specializes in device simulation. It has been used in the past for 2D modelling of non-neutral plasma in a Penning-Malmberg configuration[53–57] and partially magnetized ExB quasi-neutral plasma in a Hall-thruster configuration[26].

PEC2PIC is developed in modern FORTRAN with an Open-MP parallelization. Its functioning components are - a maneuverable Cartesian grid that can be numerically adapted to produce any desired conducting boundary profiles[58], a first order Cloud-in-cell (CIC) scheme for charge distribution to grid[59], an Successive Over Relaxation (SOR) Poisson solver parallelized by the red-black scheme[60,61], the inverse of the first order CIC for field interpolation to particles[59], and a first order Chin's exponential splitting scheme for particle pushing[62,63]. Detailed outline of these numerical schemes are available in earlier works[53,54,58].

Benchmarks for PEC2PIC include demonstrating numerical convergence with linear analytical results for a wide range of plasma instabilities including azimuthal Kelvin-Helmholtz modes and radial Bernstein modes in cylindrical pure electron plasma[53,54], and ion-resonance (two-stream) instabilities in two-component non-neutral plasma[55]. Electron Cyclotron Drift Instability (ECDI) modelling in a quasi-neutral Hall-thruster plasma showed reasonable agreement with corresponding planar linear theory, considering the device curvature and inhomogeneity of the magnetic field in the simulation[26].

For all the above experiments additional convergence tests were performed with respect to particles-per-cell (ppc) and/or mesh resolution to verify the fi-

delity of the code's output over longer periods (nonlinear phases)[26,53,55].

PEC2PIC features an integrated Monte-Carlo-Collision (MCC) routine for simulating collisional interaction of the plasma with background neutrals[64]. The MCC is based on the established model by Vahedi and others[65–68] with an improved scattering formula[69].

Past experiments using the 2D3v PIC-MCC version of PEC2PIC include modelling the destabilization of a rotating electron column by impact ionization of background neutrals[57], and investigating the effects of non-ionizing electron scattering by neutrals in cylindrical electron plasma[56]. The execution of the MCC was tested for correctness of collision statistics and collision dynamics for all simulated types of collisions[56–58].

In this experiment the MCC is used to ionize the argon background neutral gas and sustain the discharge in the cylindrical magnetron through electron impact ionization. It also adds elastic electron scattering effects when invoked.

Ion-neutral collisions of the elastic and charge exchange types are also part of the simulation. However since ion-neutral interactions are insignificant for the present results, these collisions are not taken up in the study.

C. Simulation parameters

The simulations of this paper are performed on a 250×250 Cartesian grid spanning an area, 3cm by 3cm. The circular device boundaries are numerically carved inside this square grid. The mesh resolution $\Delta x = 0.12\,mm$ is adequately small to resolve the density and field structures by more than an order of length; the latter length scales being in the range of a few mm to a few cm. Fig. 2 shows the resolution of the local Debye lengths on the mesh at different stages of the instability. The $0.12\,mm$ resolution ensures that at every time-step in the simulation period all or at least a significantly large fraction of cells resolve their respective local Debye lengths. The mesh also resolves the electron gyro-radius for velocities as low as $3.17 \times 10^5\,m/s$. Bulk electrons in the simulations have typical velocities $\mathcal{O}(10^6)\,m/s$. Hence numerical anisotropic heating associated with unresolved electron Larmor radii[70] are negated.

The simulation time step is $\delta t = 5\,ps$. The δt resolves the electron gyroperiod, $T_{ce} = 2.38\,ns$ and the local plasma oscillations periods, $T_{pe} \gtrapprox 0.25\,ns$. Here the lower limit for T_{pe} is estimated from the highest electron density values observed in simulation, $n_e \approx 2 \times 10^{17}\,m^{-3}$. The δt satisfies the Courant–Friedrichs–Lewy (CFL) condition on the Δx grid for hypothetical velocities as large as $2.4 \times 10^7\,m/s$. Typical electron velocities from the simulation are only $\mathcal{O}(10^6)\,m/s$. Hence CFL stability is ensured.

The experiment begins with zero particles in the simulation domain. The pulsed injection supplies primary electrons and the ionizing collisions produce electron-ion pairs that form the discharge. The collision cross-sections and spatial distribution of the pair-production events are determined in-situ by the PIC-MCC works. The circular conducting walls act as sinks for charged particles that come in contact. So it is evident that the particles-per-cell (ppc) in such a model will be an evolving quantity. A super particle weight, $n_w = 1.513 \times 10^7$ for both electrons and ions, ensures the presence of 15-60 ppc in the annular domain through most of the evolution in Sec III. Even in the early formative stage of the discharge (at $t < 0.2\,\mu s$) there are 5-10 ppc present.

The collision time step used in the MCC is $\Delta t_c = 4\delta t$. In Sec III and IV only ionizing collisions between electrons and neutrals are simulated while in Sec V electron-neutral collisions of the ionizing as well as the non-ionizing types (elastic and excitation collisions) are included. In the context of this paper ionizing collision implies the first ionization of Ar to form Ar^+ and excitation collision implies the first level excitation of the neutral Ar atom.

In the MCC the probability of a collision, P_c is calculated using the electron-argon collision cross-section function $\sigma_c(E_k)$, where E_k is the electron kinetic energy[68]. For exclusively ionizing collisions the σ_c maximizes for electron velocity, $v \approx 5 \times 10^6\,m/s$ i.e. $70eV$. In the presence of elastic, excitation, and ionizing collisions, σ_c becomes maximum at $v \approx 3 \times 10^6\,m/s$ i.e. $25eV$. The corresponding maxima in the collision probability calculated for $40\,mTorr$ Ar-pressure and Δt_c time interval, are $P_c = 0.004$ when non-ionizing collisions are suppressed, and $P_c = 0.011$ for the elastic, excitation, and ionizing collisions combined. Both these maxima in P_c satisfy the condition $P_c < 0.095$ set by Vahedi et al[65] for adequate representation of collisions in an MCC scheme. Hence the possibility of under-representing the electron-Ar collisions is eliminated from the experiments in the following Sections, III, IV, and V.

III. MODIFICATION OF THE SPOKE BY THE EVOLVING RADIAL ELECTRIC FIELD IN THE DEVELOPING DISCHARGE

We simulated the breakdown and nonlinear evolution of a partially magnetized ExB argon discharge in the cylindrical magnetron configuration.

In this model the electrons ionize the gaseous background but do not engage in non-ionizing scattering with the neutrals. The artificial suppression of the non-ionizing electron-neutral interactions is achieved by absorbing the elastic and excitation collision probabilities into the no-collision probability of the MCC algorithm. Tuning out the phase mixing and energy dissipation effects of elastic electron scattering produces more perceptible correlations between the nonlinear spoke structures and the evolving plasma density, density gradients, and radial electric fields in the simulations. It also helps to

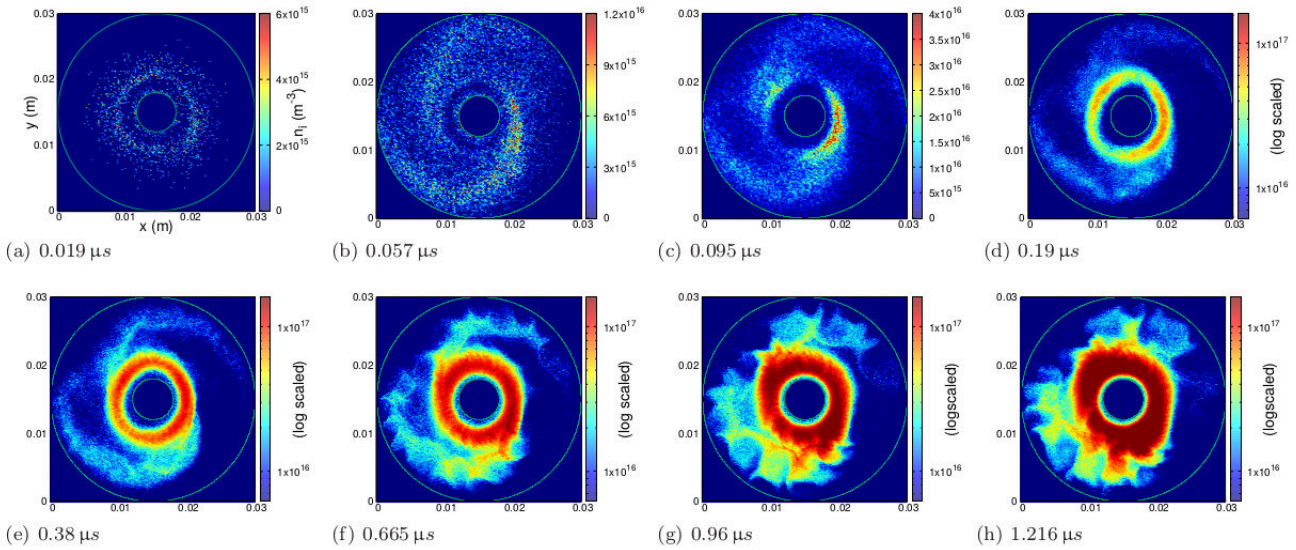

(a) 0.019 μs (b) 0.057 μs (c) 0.095 μs (d) 0.19 μs

(e) 0.38 μs (f) 0.665 μs (g) 0.96 μs (h) 1.216 μs

FIG. 3: Evolution of the ion density function, n_i at 40 mTorr Ar-pressure: (a)-(b) are in the linear phase and (c)-(h) are in the nonlinear phase of of the plasma evolution.

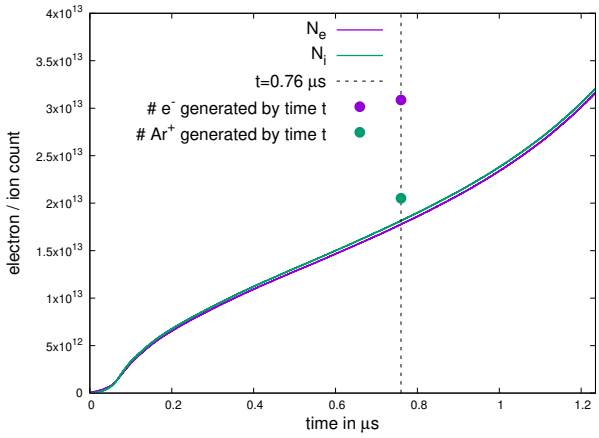

FIG. 4: [40 mTorr Ar-pressure] The number of confined electrons N_e, and confined ions N_i in the device are plotted as function of time. The cumulative count of all electrons and ions introduced in the system by $t = 0.76\,\mu s$ (confined as well as lost) are marked on the plot.

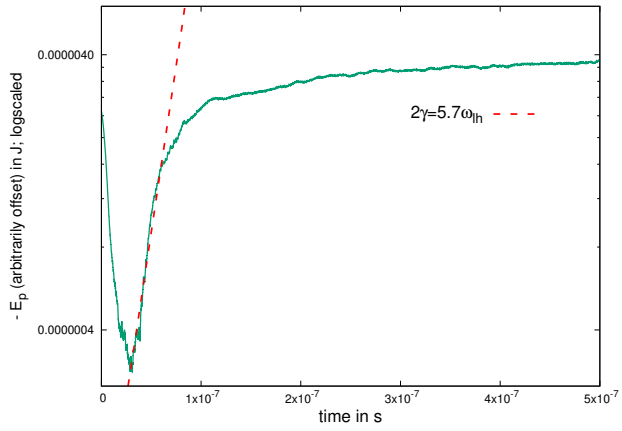

FIG. 5: [40 mTorr Ar-pressure] Electrostatic energy, E_p is plotted as a function of time. The plot is actually of an arbitrarily offset $-Ep$ which enables a log scaling of the y axis. The red dashed line is an exponential fit for the linear growth rate of the energy, 2γ.

distinguish the effects of the elastic electron scattering on the instability when the experiment is repeated with the non-ionizing collisions modelled in Sec V (see Fig. 28).

The evolution of the plasma is followed using a time-lapse of the ion density function, n_i for the simulation period $1.235\,\mu s$, shown in Fig. 3. Although not plotted here, the electron density, n_e has overlapping profiles with n_i, except in the region of the cathode sheath which is predominantly ions. The ion sheath can be seen as a low density ring of ions hugging the cathode in Fig. 3f-g.

The inner cathode is an electron source radiating electrons intermittently (Fig. 1a-b) at $2.3 \times 10^6\, m/s$ into an uniform background of argon neutrals at $40\, mTorr$ pressure. The discharge strikes at a radial ionization distance of roughly $4\frac{1}{2}$ electron gyro-radii from the release surface of the electrons ($r = 4.2\, mm$). The nascent discharge is a is a low density ($n_i \sim \mathcal{O}(10^{15})\, m^{-3}$) hoop of quasi-neutral plasma formed on the $r \approx 8\, mm$ surface (Fig. 3a-b).

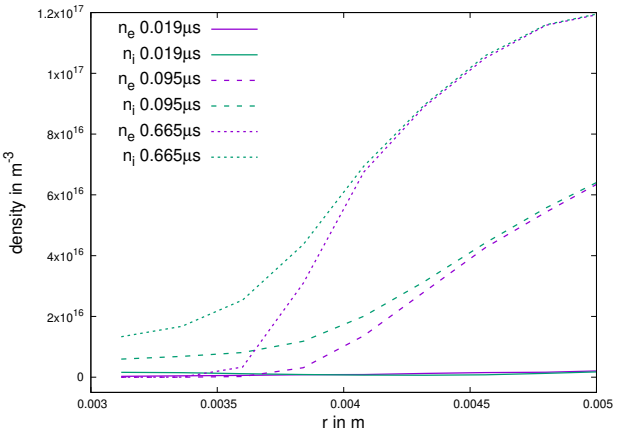

FIG. 6: [40 mTorr Ar-pressure] The formation of the cathode sheath: The radial density profiles of ions, n_i and electrons, n_e in the near cathode region are plotted at different stages of the ion sheath's formation.

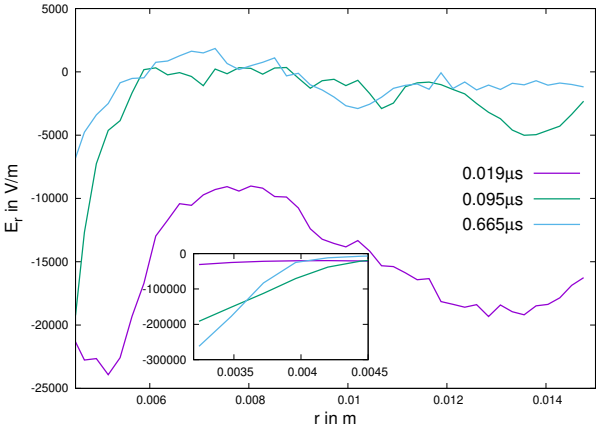

FIG. 7: [40 mTorr Ar-pressure] : Azimuthally averaged profiles of the radial electric field E_r are plotted between the walls at different stages of the instability. (Inset) The same profiles are zoomed-in on the cathode-sheath region

The circular strip of plasma has sharp radial density gradients on its inner (towards cathode) and outer surfaces. Absence of the cathode sheath (see the annular void in the ion density profile between the cathode and the circular strip in Fig. 3a-b) exposes the nascent discharge to large, near-cathode radial electric fields. On the outer surface the radial electric field and radial density gradients are co-aligned making this surface excitable to a lower hybrid type instability. The instability manifests as a rotating $m = 2$ mode emanating from the outer

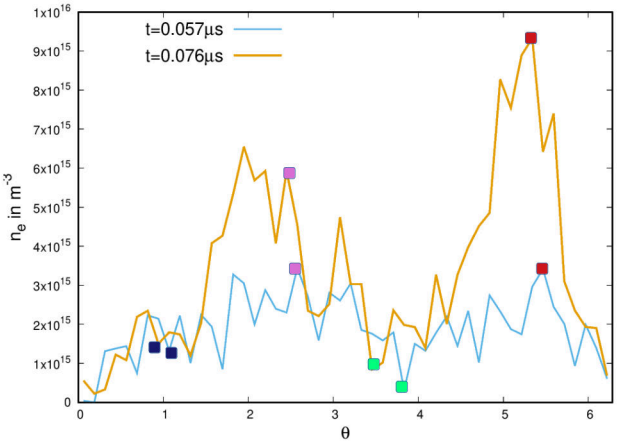

FIG. 8: [40 mTorr Ar-pressure] The azimuthal profile of electron density n_e is plotted for two closely spaced time frames in the linear phase. Each coloured marker on the two plots identifies a particular propagating phase.

plasma surface (Fig. 3b).

Fig. 3c-d are in early nonlinear phase of evolution. The profile is now visually separable into an inner core of density $\mathcal{O}(10^{17})\, m^{-3}$ and a protruding $m = 2$ spoke of density $\mathcal{O}(10^{16})\, m^{-3}$. An ion sheath has started forming partially shielding the cathode. The radial field reduction has an immediate impact on the spoke, halting its linear growth and stagnating its azimuthal propagation.

Fig. 3e-f are further ahead in the nonlinear phase. A fully developed ion sheath now drops the bulk of the applied dc voltage leaving only a weak electric field in quasi-neutral plasma, saturating the growth of the $m = 2$ mode. A polar section of the profile in Fig. 3e-f has five distinct radial density layers - i) ion sheath ($n_i \sim 2 \times 10^{16}\, m^{-3}$), ii) bulk plasma or core ($n_i \sim 10^{17}\, m^{-3}$), iii) a low density bay between the core and the spoke's arm ($n_i < 10^{16}\, m^{-3}$), iv) the spoke arm ($n_i \sim 2.5 \times 10^{16}\, m^{-3}$), and v) a low density near-anode distribution $n_i < 10^{16}\, m^{-3}$.

With radial electric fields getting dammed inside the cathode sheath, the long wavelength $m = 2$ mode starts to disintegrate. Faults starts developing on the spoke's outer surfaces that eventually wedge inwards breaking the spoke into short wavelength "spoke-on-spoke" modes, visible as density spikes on the spoke-arms in Fig. 3e-f. The wave-breaking proceeds inwards from the spoke outer layer because the surface of the wave has the maximum local electric fields and density gradients making it unstable.

Fig.3g-h are in the advanced nonlinear stage of the instability. At this stage the long wavelength spoke has collapsed leaving on the short scale structures. The nonlinear cascade of energy from the long to short wavelength is complete.

The transition of the spoke mode to a shorter wavelength scale with the waning of the electric field. This is

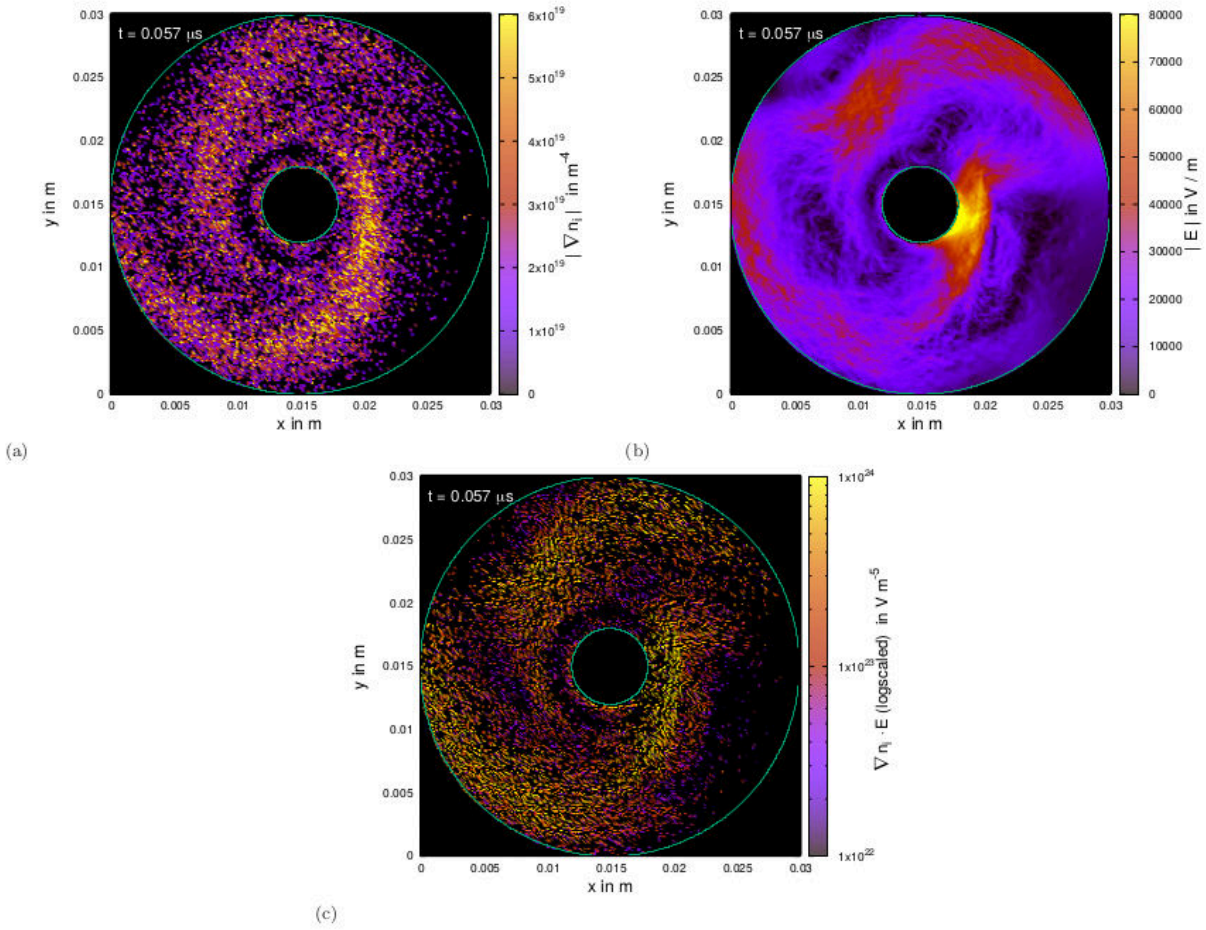

FIG. 9: [40 mTorr Ar-pressure] Density gradients and fields at $t = 0.057\,\mu s$ (linear stage): (a) is a map of the magnitude of 2D ion density gradient, $|\nabla n_i|$. (b) is a map of the magntidue of 2D electric field $|E|$. (c) is map of the scalare product $\nabla n_i \cdot E$.

not surprising as recent parametric studies on the lower hybrid instability have demonstrated that at low electric fields its linear dispersion curve starts trending towards an ion sound instability dispersion, with the wavelength of the excited modes getting shorter and comparable to the electron gyro radius[33,49]. In this experiment the electrons riding the "spoke-on-spoke" structures in Fig.3g-h have around $20\,eV$ of energy, which implies a net velocity of $2.65 \times 10^6\,m/s$. Out of this, the guiding centre drift accounts for $0.66 \times 10^6\,m/s$ and the rest $2 \times 10^6\,m/s$ goes into the gyro motion. An approximate Larmor radius of these electrons is thus $\sim 0.75\,mm$. The length-scale of the observed short modes measure $\sim 3\,mm$, which is about four gyro-radii. So the mode transition can be perceived as a nonlinear extension of a fundamental linear property of the instability.

All through the experiment in Fig. 3a-h, a radial expansion of the core distribution occurs in response to the algebraic increase of the pair population plotted in Fig. 4. The ion populations remain a touch above that of electrons, to produce the non-neutral cathode sheath. To quantify the particle loss processes in the discharge the total number of electrons introduced through injection and ionization, and the total number of ions generated through ionization by the nonlinear stage $t = 0.76\,\mu s$ are marked on Fig. 4. It is evident that by this time nearly half (43%) of the electrons that were at some point of time part of the system have been lost through radial transport to the walls. In comparison ion retention is significantly higher with a loss fraction of 12% of the total generated number. It will be later discussed how the electrons are transported anomalously while the unmagnetized ions are transported to the walls by the radial electric fields.

Fig. 5 is a plot of the net electrostatic energy, E_p as a function of time. To focus on the phase transitions in the curve, the saturated phase is plotted only up to $0.5\,\mu s$. For logarithmic scaling the sign of the negative electrostatic energy has been flipped. The initial fall of the curve is a transient phase of non-neutrality when the space is occupied by mostly injected electrons ($t < 0.025\,\mu s$). This is followed by a linear growth

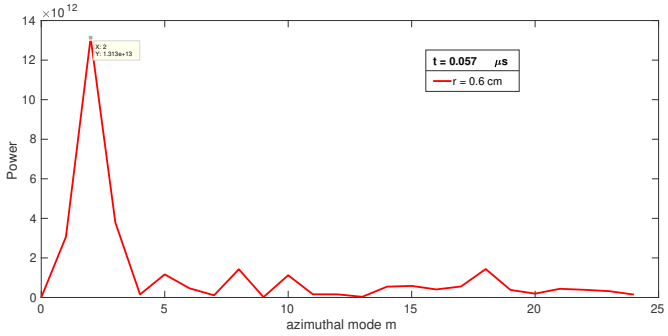

(a)

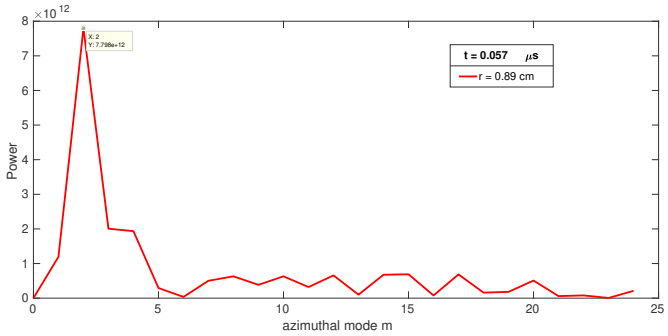

(b)

FIG. 10: [40 mTorr Ar-pressure]. FFT of the azimuthal electron density on radial surfaces, (a) $r = 0.6\,cm$ and (b) $r = 0.89\,cm$ at $t = 0.057\,\mu s$ (linear stage).

of the lower hybrid instability from $0.025\,\mu s$ to $0.075\,\mu s$ (Fig. 3a-b). The growth rate of E_p is measured using exponential fitting (see red dotted curve) to be $5.7\omega_{lh}$, where $\omega_{lh} = \sqrt{\omega_{ce}\omega_{ci}} = 9.777 \times 10^6\,rad/sec$ is the lower hybrid frequency. As E_p is a second order quantity the linear growth rate of the $m = 2$ mode is $\gamma = 0.5 \times 5.7\omega_{lh} = 2.786 \times 10^7\,rad/sec$. The linear phase transits into a nonlinear "knee" of the curve in the interval $0.075\mu s < t < 0.12\,\mu s$ when the growth is checked by a developing cathode sheath (Fig. 3c-d). The range $t > 0.12\,\mu s$ (Fig. 3e-h) is the saturation phase when the cathode sheath has fully developed.

Fig. 6 shows the development of the cathode sheath which modulates the rotating spoke's wavelength. Radial density profiles of electrons and ions are plotted in the near-cathode region from three stages of the evolution - i) the linear growth stage (time-frame a of Fig. 3) ii) the knee of the saturation (time-frame c of Fig. 3) and iii) the saturated phase (time-frame f of Fig. 3). In the linear stage electron and ion densities near the cathode are low and almost equal. At the knee of the transition, the ion density exceeds the electron density near the cathode by $\Delta n = 0.8 \times 10^{16}\,m^{-3}$. In the saturated stage the differential density in the sheath has risen even higher to $\Delta n = 1.4 \times 10^{16}\,m^{-3}$.

The effect of the developing ion sheath on the radial electric field, E_r is shown in Fig.7. The same three time-frames as Fig.6 are used in Fig. 7 to plot the E_r function. The main figure shows the E_r profiles in the quasi-neutral bulk while the the inset shows the E_r in the cathode sheath region. In the linear stage, E_r in the bulk is around $1.25 \times 10^4\,V/m$. In the knee of the growth its value has diminished to about $3000\,V/m$ and in the saturated state it goes down further to about $1000\,V/m$. E_r in the sheath (Fig. 7 inset) has an antagonistic evolution getting stronger as the sheath develops.

The observations in Fig. 6 and 7 are consistent with spoke's evolution in Fig. 3.

In this experiment the long scale $m = 2$ mode does not make a full 2π rotation before its growth is arrested and its propagation stagnated by the field reduction in the plasma. As a result, the usual Fast-Fourier-transform (FFT) methods for mode frequency estimations[53,55] are not applicable. We used an alternative method of frequency measurement using mode phase traces on the azimuthal profiles of electron density. Fig. 8 shows the evolution of the azimuthal n_e at $r = 0.768\,cm$ in two close time-frames, $t = 0.057\,\mu s$ (Fig. 3b) and $t = 0.076\,\mu s$. It is assumed that the shape of the azimuthal density profile is not significantly altered between these frames. The pairs of same colored dots are the phase traces in the clockwise propagation of the mode. Applying forward differences, the traces yield an average angular frequency, $\omega = 1.023\omega_{lh} = 1 \times 10^7\,rad/sec$.

All parameters of the lower hybrid instability viz., the plasma density, its gradient, and the radial electric field, have non-uniform profiles between the radial walls. Hence a straight one-to-one mapping of the macroscopic linear phase results from Fig. 5 and 8, to a localized analytical model of the lower hybrid instability is not possible. This aspect is further elaborated in the Appendix.

In Subsections A, and B we take a closer look at the excitation mechanism and the particle transport effects of the long wavelength $m = 2$ spokes, and the short-scale spokes respectively.

A. Conditions for the long wavelength spoke and its plasma transport

Excitation of the $m = 2$ mode and the plasma transport caused by it are investigated by analyzing the state of the plasma in the linear phase time-frame $t = 0.057\,\mu s$ (Fig. 3b).

Analytical theory suggests that a quasi-neutral plasma surface possessing strong, collinear electric field and density gradient perpendicular to the magnetic field will be susceptible to the lower hybrid instability.

In Fig. 9 we test the lower hybrid instability hypothesis for the spoke. Here we have plotted 2D color maps of three parameters a) the scalar ion density gradient $|\nabla n_i|$, b) the magnitude of local electric field, $|E|$ and c) the scalar product function $\nabla n_i \cdot E$. The plots reveal that the base of the spoke is the quasi-neutral surface with the maximum electric field and density gradient, in near

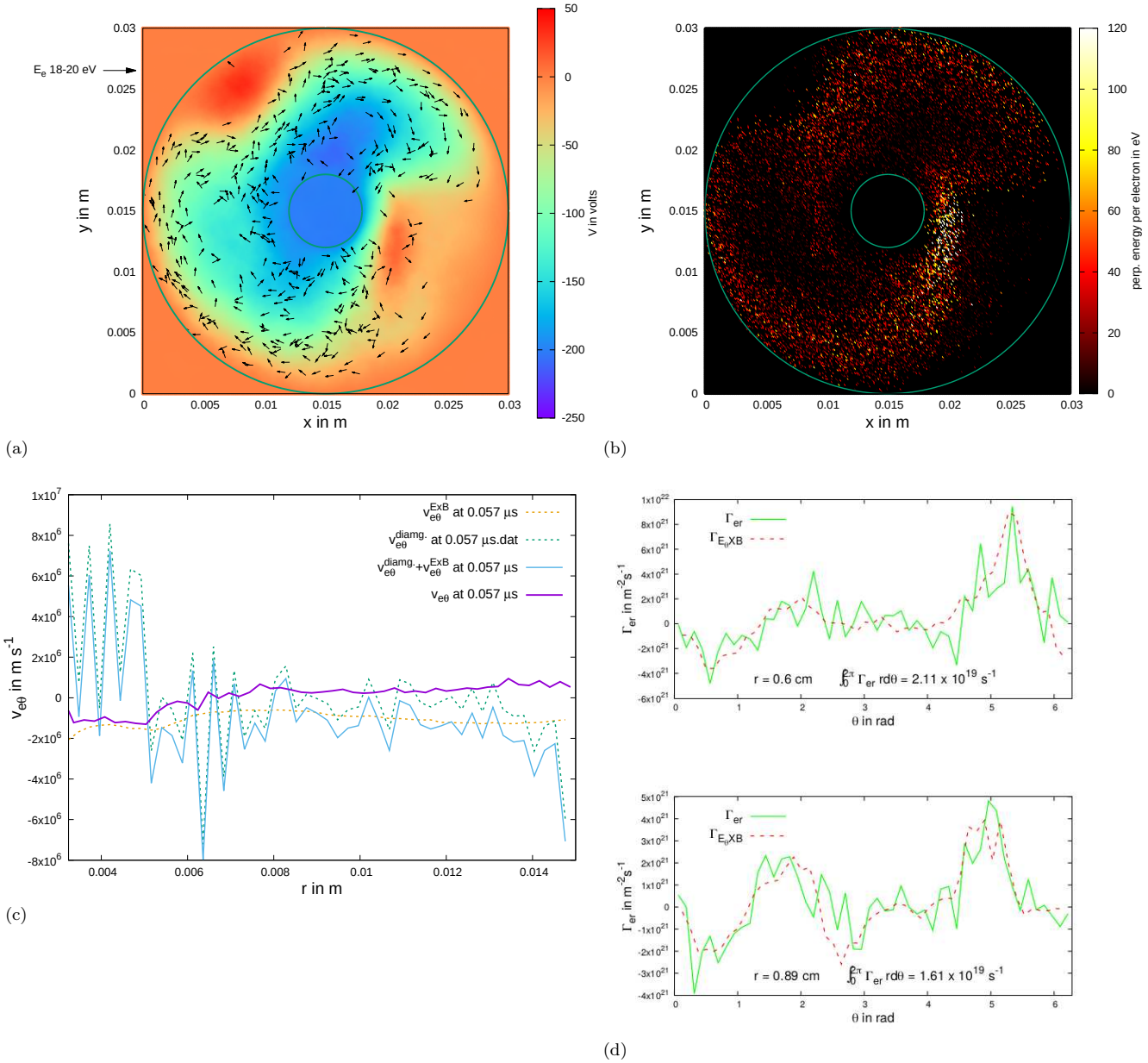

FIG. 11: [40 mTorr Ar-pressure] Electron dynamics in the linear stage ($t = 0.057\,\mu s$): (a) is a colour contour of the potential V. A vector plot of electron flow in the 18-20 eV range (exact magnitudes undepicted) is superimposed. (b) is a map of the perpendicular i.e. on plane kinetic energy of electrons (c) is a plot azimuthal electron velocity as a function radius. $v_{e\theta}$ is the measured velocity, $v_{e\theta}^{E\times B}$ and $v_{e\theta}^{diamg.}$ are the calculated $E \times B$ drift and diagmagnetic drift at the radial locations. (d) The radial electron flux density , Γ_{er} is plotted on two radial surfaces, (top) $r = 0.6\,cm$, and (bottom) $r = 0.89\,cm$. The red dashed lines represent the calculated anomalous flux density $\Gamma_{E_\theta \times B}$ on the two surfaces. The total electron flux on the surfaces are also printed on the figures.

parallel alignment. This confirms that the $m = 2$ spoke is indeed a linear mode of the lower hybrid instability.

In Fig. 10 we have performed angular FFT's of the azimuthal electron density functions at a) a radial surface at the spoke's base, $r = 0.6\,cm$ b) a radial surface inside the spoke's distribution, $r = 0.89\,cm$. Both transforms are similar, showing a sharp peaks at $m = 2$ and negligible power at all other mode numbers. This indicates that a linear, pure $m = 2$ gets excited globally in the cloud.

Fig. 11a is a map of the potential function at $t = 0.057\,\mu s$. Using the corresponding density snapshot, Fig. 3b as a reference, it can be deduced that the in-

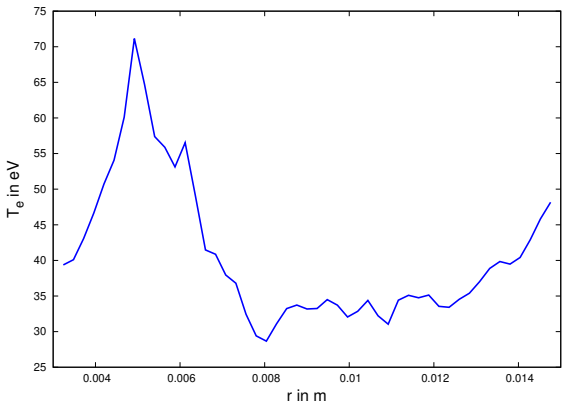

FIG. 12: [40 mTorr Ar-pressure] Radial profile of electron temperature, T_e at $t = 0.057\,\mu s$ (linear stage).

ner blue (Azure blue) region in Fig. 11a with potential $V \sim -200\,V$ is the plasma core, and the outer green (sea foam green) area with potential $V \sim -100\,V$ represents the spoke. Areas with shades of orange or red represent regions with positive potential values. The transition layers between negative and positive potentials are double-layers with significant local electric fields.

A vector map of the planar electron velocities (with drift and thermal components) in the 18-20 eV range, is superimposed on the potential map in Fig. 11a, to illustrate the ExB rotation of electron along the double layers. Note that the vectors in Fig. 11a are all scaled to the same magnitude, hence they posses only the information of direction

Fig. 11b maps the full spectrum of perpendicular electron velocities. As expected, the transition layers of the potential map (Fig. 11a) are the regions of major ExB streaming of electrons in Fig. 11b. The high-energy yellow patch to the right of the cathode in Fig. 11b, corresponds to the base of spoke in Fig. 9b. Electron velocities in this patch are naturally highest because this region has the maximum electric field, evident from Fig. 9b.

In Fig. 11c we studied the rotational drift dynamics of electrons in the linear phase. There are two azimuthal drifts at work; i) the $E_r(r)\times B$ drift of the guiding centre, where $E_r(r)$ is the radial electric field and ii) the diamagnetic $\nabla P_e(r)\times B$ drift of the electron fluid, where $P_e(r)$ is the electron gas pressure, assumed to be a function of the radial coordinate only. Radial profiles of the two angular drift velocities, $v_{e\theta}^{E\times B}$ and $v_{e\theta}^{diamg}$ are plotted as dashed curves in Fig. 11c. To calculate the radial pressure gradient the expression $\frac{\delta P_e}{\delta r} = k_B T_e \frac{\delta n_e}{\delta r} + k_B n_e \frac{\delta T_e}{\delta r}$ is used, where $n_e(r)$ and $T_e(r)$ are the azimuthally averaged electron density and electron temperature respectively, while k_B is the Boltzmann constant. The local variations of the electron temperature (Fig. 12) and density lend $v_{e\theta}^{diamg}$ its local fluctuations.

The sum of the drift components $(v_{e\theta}^{E\times B} + v_{e\theta}^{diamg})$ is plotted as a solid cyan line in Fig. 11c. This can be compared with the measured azimuthal velocity of electrons, $v_{e\theta}$, plotted as a solid purple line. The two curves are not convergent but have an average agreement in their profiles. The measured angular velocity $v_{e\theta}$ has a much smoother profile than the sum of the drift components $(v_{e\theta}^{E\times B} + v_{e\theta}^{diamg})$.

We now focus on the anomalous radial transport of electrons caused by the $E_\theta \times B$ drift where E_θ is the azimuthal wave field. The transport is quantified using the electron flux density on a radial surface defined as $\Gamma_{er} = n_e(\theta)v_{er}(\theta)$, where n_e and v_{er} are local density and radial velocity of electrons on the surface. In Fig. 11d the Γ_{er} function at $t = 0.057\,\mu s$ is plotted on the radial surface of the spoke's base, $r = 0.6\,cm$ (Fig. 11d upper plot) and a surface inside the spoke $r = 0.89\,cm$ (Fig. 11d lower plot). Γ_{er} is compared with the flux density function estimated from the $E_\theta \times B$ drift velocity given by, $\Gamma_{E_\theta\times B} = n_e E_\theta / B$. The plots show a high level of convergence between the measured and estimated electron flux densities, demonstrating that the radial transport is completely anomalous. Further the shapes of the Γ_{er} profiles clearly indicate that the transport is maximum through the spoke arms. The net fluxes on the two surfaces, $\int_0^{2\pi} \Gamma_{er}\,(rd\theta)$ are also mentioned inside each figure. These come out to be $\mathcal{O}(10^{19})\,s^{-1}$.

The instability and ionizing collisions shape the electron temperature profile. In Fig. 12 the 3D electron temperature is plotted as a function of radius, obtained using standard deviation of electron velocities on fine radial bins. In the plasma core the T_e profile is peak shaped reaching a maximum value of $70\,eV$ at around $r = 0.5\,cm$. Inside the spoke T_e remains relatively flat hovering around the $32\,eV$ mark. Its value again rises to about $40\,eV$ in the near-anode region. It is interesting to note that despite having double layers on its surfaces and facilitating the electron radial transport, the spoke remains significantly cooler than the plasma core. The higher temperature in the core could be related to the higher plasma density in this region.

The unmagnetized argon ions can have collective motion guided by the electric field lines in the plasma. Fig. 13a and 13b are maps of the radial ion velocity v_{ir} and the azimuthal ion velocities, $v_{i\theta}$. Typical Ar^+ velocities in these distributions are in the range of a few hundred to a thousand m/s. In Fig. 13a it is evident that most of the ions are transported inward towards the cathode following the E_r. However hugging the cathode in an azimuthal segment, is a small distribution of ions with radially divergent velocities. The presence of an outward radiating segment of ions so close to the cathode in the linear stage is not well understood. It could perhaps be some transient effect; it certainly disappears at later stages once the cathode sheath is formed (see Fig.s 18a, 26a).

Fig. 13b shows that the ions experience drag from the E_θ of the linear $m = 2$ mode. Hence the $v_{i\theta}$ changes sign

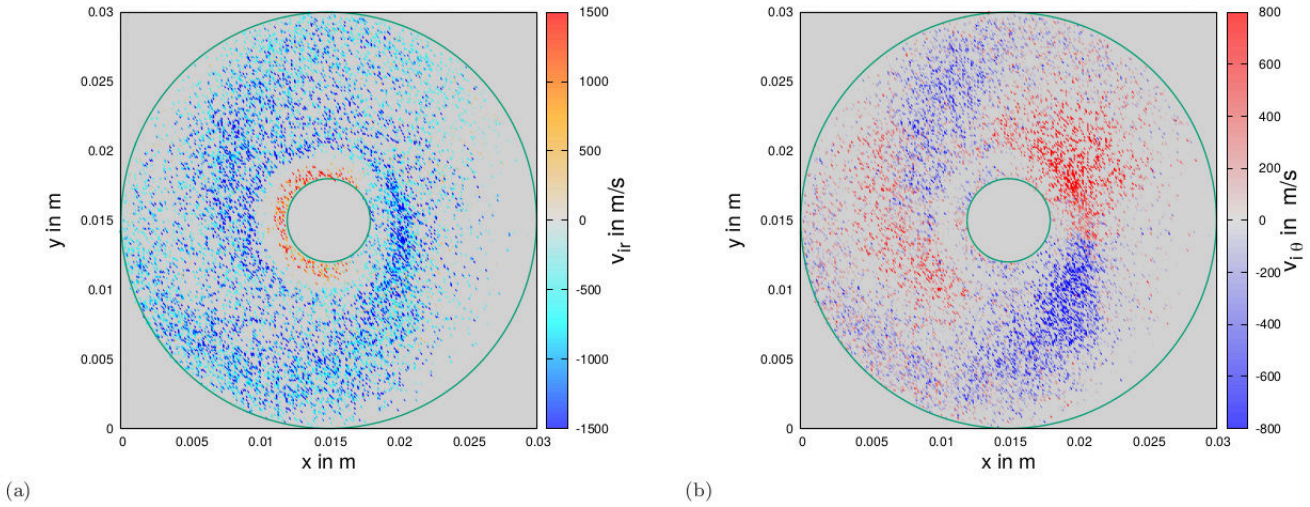

FIG. 13: [40 mTorr Ar-pressure] Ion velocity maps at $t = 0.057\,\mu s$ (linear stage): (a) is map of the radial ion velocity v_{ir}, and (b) is a map of the azimuthal ion velocity $v_{i\theta}$

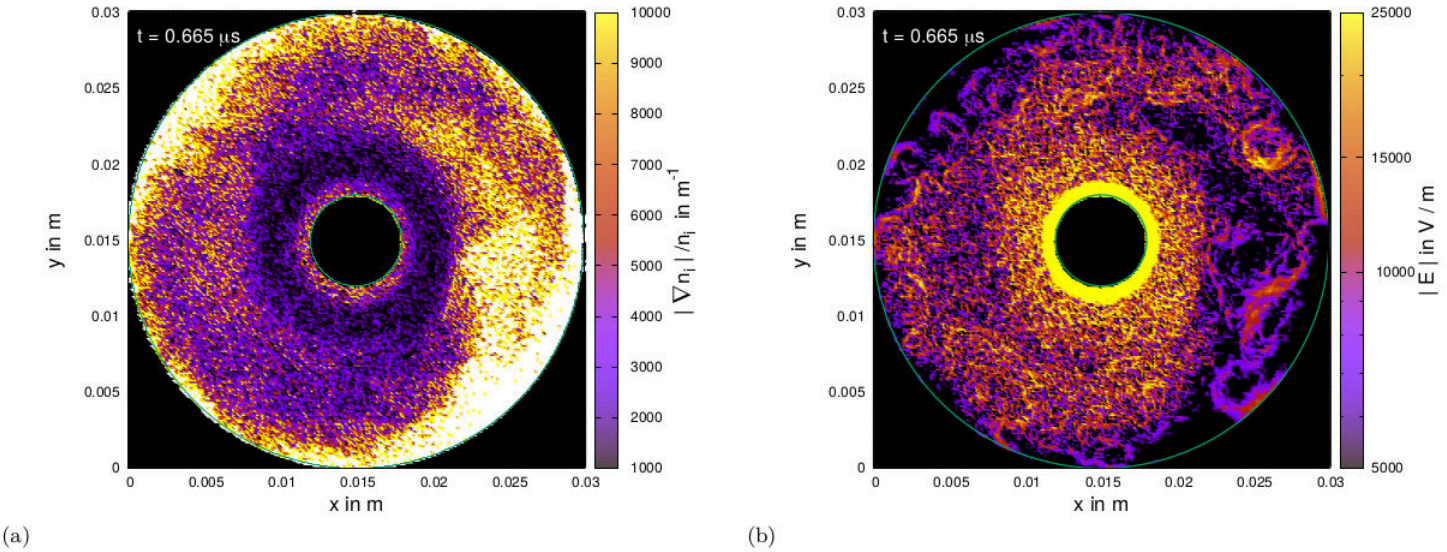

FIG. 14: 40 mTorr Ar-pressure] Density gradients and fields at $t = 0.665\,\mu s$ (nonlinear stage): (a) is a map of the magnitude of 2D ion density gradient, $|\nabla n_i|$. (b) is a map of the magntidue of 2D electric field $|E|$.

at the transitions between the crests and troughs of the perturbation, E_θ.

B. Conditions for the short-scale spoke and its plasma transport

The nonlinear short scale structures are analyzed at the time frame, $t = 0.665\,\mu s$ (Fig. 3f).

With the diminishing of the E_r in plasma, the long $m = 2$ spoke transits into these short wavelength modes. The transitions are driven by the density gradients and the wave-field on the surfaces of the long spoke.

At this stage the profile's composition includes a wide spectrum of density values (Fig. 3f). There is an order of magnitude's difference between the densities in the plasma core and the spoke distribution. To gauge the local steepness of density gradients on such a profile, it is useful to express the gradient in units of the local density. In Fig. 14a we have plotted this function, $|\nabla n_i|/|n_i|$ as a color map. The map shows distinct yellow i.e high gradient outlines on the spoke distributions. The transition of structure happens with the help of these surface gradients.

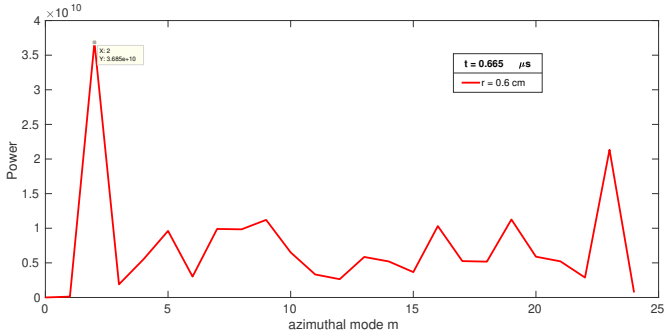

(a)

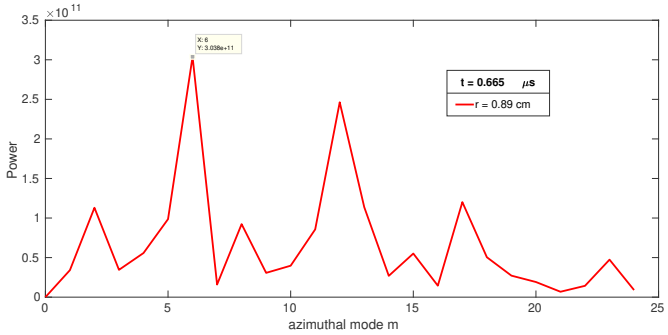

(b)

FIG. 15: [40 mTorr Ar-pressure]. FFT of the azimuthal electron density on radial surfaces, (a) $r = 0.6\,cm$ and (b) $r = 0.89\,cm$ at $t = 0.665\,\mu s$ (nonlinear stage)

.

The electric field on the long mode's surface is another contributing factor to the transition. In Fig. 14b, the local electric field's magnitude $|E|$ is mapped on the profile. On the map the spoke surface is distinctly brighter indicating the abundance of field on the structure. At $t = 0.665\,\mu s$ the long mode's field is already perturbed by the short scale modes, evident from the wavy trail of high electric field along the spoke arms.

There is high spatial correlation between the maps in Fig.s 3f, 14a, and 14b, with supports our model for the mode transition.

Fig. 15 shows an azimuthal FFT on the n_e profile at a) the spoke base, $r = 0.6\,cm$, and b) inside spoke arm at $r = 0.89\,cm$. In contrast to the linear stage FFT which gave only a single peak at $m = 2$ (see Fig. 10), Fig. 15 has multiple peaks of higher mode numbers mixed with the $m = 2$ at both radii. Moreover, in the nonlinear stage the modes' power spectrum has a higher dependency on the radius of measurement. This is understandable, as the short scale modes are nonlinear localized structures whereas the $m = 2$ was a linear global mode on the plasma cloud.

The potential function at $t = 0.665\,\mu s$ is mapped in Fig. 16a. Referring the corresponding density map, Fig. 3f, we can decipher that the the islands of red (positive potential values) in between the the blue (negative potential values) in the outer edges of the potential profile are the perturbations of the short scale structures excited on the long spoke. A uniformly scaled (in magnitude) vector plot of on-plane electron velocities in the 18-20eV range is overlaid on the potential map. The vectors show ExB circulation of electrons around the potential islands on the spoke. A couple of such vortices are highlighted with square frames in Fig. 16a. The rotational motion of electrons in the spoke at this stage can now be visualized as electrons looping around the potential islands in their clockwise flow. Some of these loops are anti-clockwise as the ones inside the square frames.

Fig. 16b is a map of the full spectrum of on-plane electron energies. Referring Fig. 16a it is evident that all double-layers in the potential map light up with higher energies in the electron kinetic energy map.

In Fig. 16c the electron flux density, Γ_{er} is plotted on two radial surfaces at $t = 0.665\,\mu s$: On the left, $r = 0.6\,cm$ (spoke's base), and on the right, $r = 0.89\,cm$ (in the spoke). The Γ_{er} profiles agree with corresponding $E_\theta \times B$ estimates, corroborating the anomalous nature of the transport. The fluctuation in the Γ_{er} in Fig. 16c have signatures of the new short scale structures. The integrated surface fluxes at this nonlinear stage (see inside Fig. 16c) are lower than in the linear stage (see inside Fig. 11d). This indicates that the spoke's transition to short length scale brings down the anomalous electron transport.

The radial profile of the electron temperature, T_e at $t = 0.665\mu s$ is depicted in Fig. 17. The plot reveals that with the the saturation of the instability plasma temperatures go down. Maximum T_e in the core plasma is now 10eV, while it was about 70eV in the linear stage. The spoke now has temperatures in the 6-7 eV range, in contrast to 32 eV while the $m = 2$ mode was growing. The lowering of electron temperature in the cloud can be attributed to the reduction of radial electric field, allowing the cloud to cool by anomalously transporting its energetic electrons to the walls.

Ion radial velocities, v_{ir} at $t = 0.665\mu s$ are mapped in Fig. 18a. In the sheath and pre-sheath regions near the cathode there is large negative E_r (refer the cyan curve in Fig. 7) which directs the v_{ir} inward. Hence there is a blue and cyan strip of negative v_{ir} values surrounding the cathode. Just outside the inner blue strip, there is a concentric orange strip of divergent v_{ir}. This is again consistent with the slightly positive values of E_r in this part of the core plasma ($0.6\,cm < r < 0.9\,cm$ in Fig. 7 - cyan curve). Ion radial velocities in the spoke have an interesting distribution of alternating positive and negative values much like their azimuthal velocities in Fig. 18b. The periodic fluctuations of the radial ion velocities show that the short scale structures are not purely azimuthal, but have a non negligible k_r component along with the k_θ in their wave-vector.

The ion azimuthal velocity $v_{i\theta}$ distribution is depicted in Fig. 18b. The $v_{i\theta}$ follows the pattern of the short scale modes, alternating between positive and negative velocities along the crests and troughs of the wave field. Hence

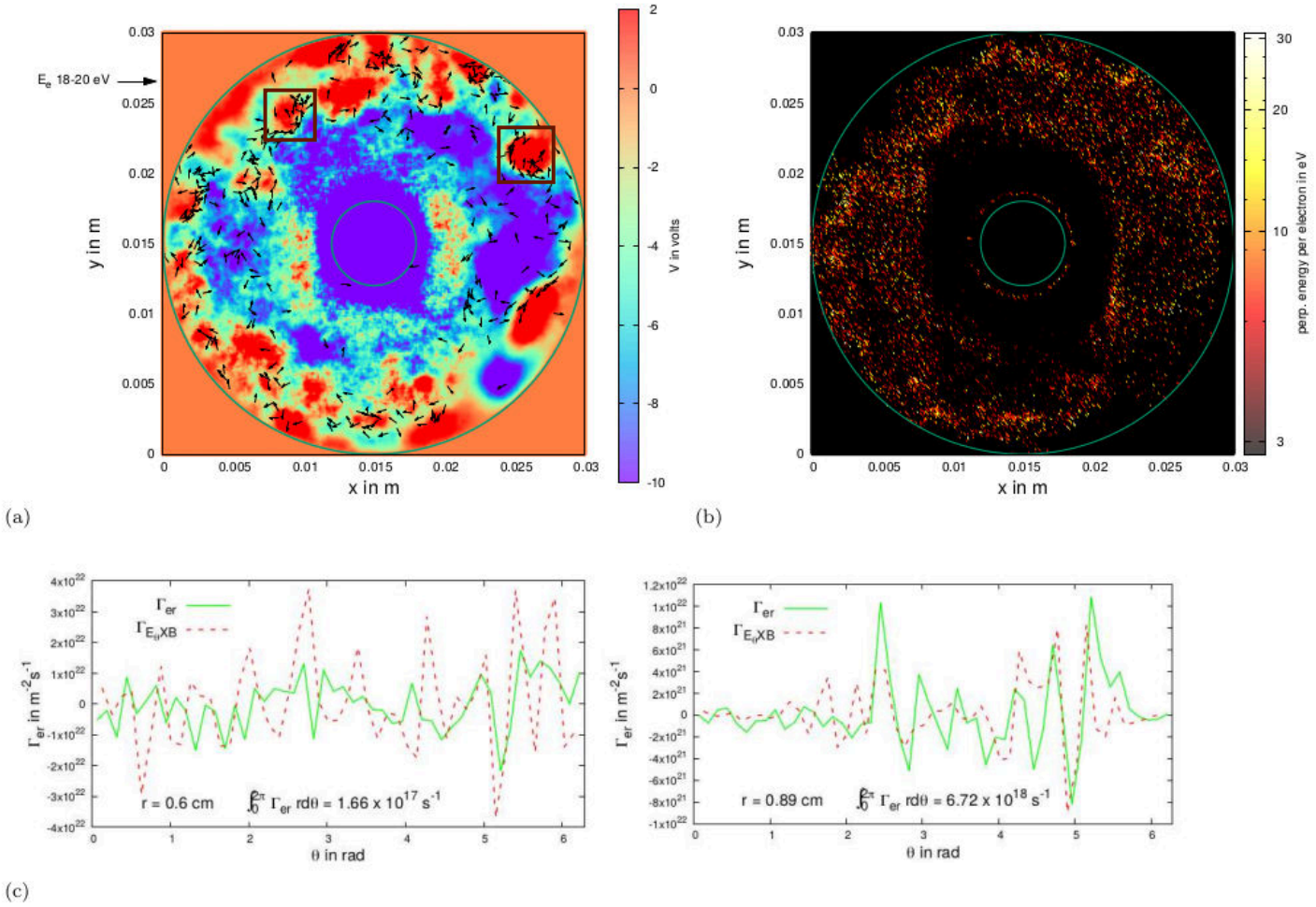

FIG. 16: [40 mTorr Ar-pressure] Electron dynamics in the nonlinear stage ($t = 0.665\,\mu s$): (a) is a colour contour of the potential V. A vector plot of electron flow in the 18-20 eV range (exact magnitudes undepicted) is superimposed. The boxes indicate electron vortices (b) is a map of the perpendicular i.e. on plane kinetic energy of electrons (c) The radial electron flux density , Γ_{er} is plotted on two radial surfaces, (left) $r = 0.6\,cm$, and (right) $r = 0.89\,cm$. The red dashed lines represent the calculated anomalous flux density $\Gamma_{E_\theta \times B}$ on the two surfaces. The total electron flux on the surfaces are also printed on the figures.

the short scale spokes, like the earlier long wavelength spoke, drag the ions azimuthally.

IV. SPOKE TRANSITIONS BROUGHT ON BY A NEUTRAL PRESSURE REDUCTION

At $t = 1.235\mu s$ the experiment at 40mTorr neutral pressure is stopped to prevent breaching the reserved array limit for particles (see Fig 4). However there is still scope for the simulation to be continued at a lower neutral pressure. Under reduced background pressure the difference between the pair production rate and particle loss rate becomes smaller, allowing the experiment to go on for at least another two micro-seconds with timely array reallocation interventions. Physics-wise the inhibition of pair production can impact the spoke structures, by reducing plasma density and enhancing the E_r penetration. We conducted this experiment by continuing the simulation from Sec III at a lower neutral pressure of 1mTorr for another $1.805\mu s$ i.e. till $t = 3.04\mu s$.

Fig. 19 shows the evolution of the ion density function after the background pressure reduction. Fig. 19a-b continue to bear the short scale modes that were excited in the latter stages of the 40mTorr experiment. In Fig.19c-d a reorganization of the cloud is observed. The radially expanding cloud engulfs all short scale structures, replacing them with a new azimuthal distribution that has nonlinear $m = 2$ characteristics. Through Fig. 19e-h the elliptical cloud gradually takes on a spiral shape that has a mixture of $m = 1$ and $m = 2$ embedded in its structure. Similar intriguing spiral structures have been observed in

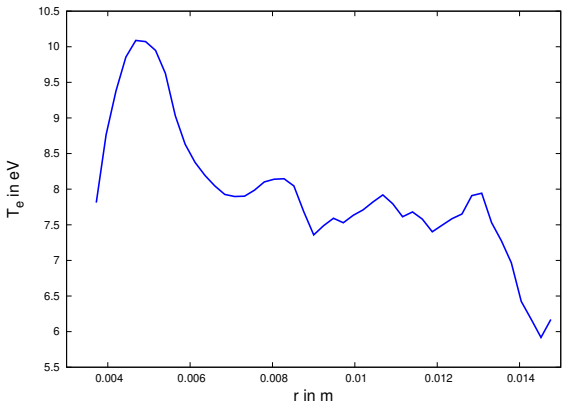

FIG. 17: [40 mTorr Ar-pressure] Radial profile of electron temperature, T_e at $t = 0.665\,\mu s$ (nonlinear stage).

other experiments on rotating spoke modes[39,41,71–73].

In Fig. 20 the evolution of the resident electron and ion populations are plotted from $t = 0$ to $t = 3.04\,\mu s$ with a red dotted line indicating the time of pressure transition. Scaling down the neutral pressure by $\frac{1}{40}$ causes a sharp transition in the population curve to a more relaxed growth.

The shortage of neutrals induces a turbulent redistribution of the radial density with the plasma rushing outward to compensate the outer wall losses. The process stretches the cloud and its sheath thin. In Fig. 21 the cathode sheath population is shown at time frames corresponding to Fig.s 19b, 19d, and 19f. Here the sheath's evolution is just the inverse of Fig. 6. A disintegration of the ion sheath is in effect. Between $t = 1.53\mu s$ (Fig. 19b) and $t = 2.612\mu s$ (Fig. 19f) the differential density in the sheath falls from $\Delta n = 3 \times 10^{16}\,m^{-3}$ to about $\Delta n = 2 \times 10^{16}\,m^{-3}$.

The sheath's disintegration in turn directly impacts the E_r penetration in the plasma. In Fig. 22 the E_r profiles in the bulk plasma are plotted for the same three time-frames as Fig. 21 with the inset showing the E_r profiles in the sheath region. The sheath's shielding weakens with the plasma expansion leading to a lowering of E_r in the sheath and a rise of E_r in the quasi-neutral bulk. Between $t = 1.53\mu s$ (Fig. 19b) and $t = 2.612\mu s$ (Fig. 19f) the radial electric penetrating the quasi-neutral region has increased by a magnitude of $\sim 5000\,V/m$.

With the help of Fig.s 21 and 22 we can attempt a simplistic model for the nonlinear reemergence of a long spoke when the neutral pressure is reduced: A turbulent radial expansion of the plasma is induced by the arrested neutral supply. The cloud gets stretched, which partially disintegrates the sheath leading to radial electric field leaking into the quasi-neutral plasma. Linear theory shows that higher electric fields produce longer spokes. Hence the spoke naturally transitions from short scale back to a long scale when the pressure is reduced.

We investigated the effects of the nonlinear spiral spoke, by analyzing the time frame $t = 2.612\mu s$ (Fig. 19f). Fig.s 23a and 23b are azimuthal FFTs of the n_e distributions on $r = 0.6\,cm$ and $r = 0.89\,cm$ respectively, performed at $t = 2.612\mu s$. Both spectra show a broad multi-peaked structure between $m = 1$ and $m = 6$. This implies that the spiral spoke structure is for the most part, a mixture of the long wave lengths $1 \leq m \leq 6$. The power spectra also have few peaks in the short wavelength region, $m \geq 10$.

Fig. 24a is a plot of the potential function at $t = 2.612\mu s$. The small sized equipotent islands of Fig. 16a, are now replaced by fewer islands of relatively larger dimensions. A vector plot of the planar electron velocities in the range 18-20eV in Fig. 24a, shows that electrons drift clockwise in an inward spiral path through the transition layers between the islands. A map of the planar kinetic energies of electrons in Fig. 24b, demonstrates the same constricted ExB flow of electrons through narrow double layer channels between the potential islands.

In Fig. 24c the anomalous electron transport at $t = 2.612\mu s$ is depicted in the form of the flux density function, Γ_{er} on the radial surfaces $r = 0.6\,cm$ and $r = 0.89\,cm$. Similar to Fig.s 16c and 11d these Γ_{er} profiles are in reasonable agreement with their corresponding drift estimations, $\Gamma_{E_\theta \times B}$. The larger values of the integrated surfaces fluxes in Fig. 24c compared to Fig. 16c, implies that the spoke's transition back to a longer length scale, has re-intensified the anomalous transport process.

The 3D electron temperature profile at $t = 2.612\mu s$ is plotted in Fig. 25. The curve falls monotonically from 28eV in the core to about 10eV at the outer edge of the spoke. The higher temperatures in the profile of Fig. 25 compared to that in Fig. 17, shows that electrons everywhere in the cloud were heated by the turbulence of the plasma expansion following the neutral pressure reduction.

The radial velocities of ions at $t = 2.612\mu s$ are mapped in Fig 26a. The electrostatic expansion of the plasma cloud has a distinct impact on the v_{ir} distribution. Density gradient driven forces pull all but the most deep seated ions in the cathode's potential well, in the radially outward direction. This splits the v_{ir} distribution into two domains, viz., a cathode clinging domain of negative radial velocities composed of ions at high negative potentials, and an outer domain of positive radial velocities composed of ions moving with the expanding cloud. The two domains are connected by a transition layer of near-zero radial velocities. The negative velocity domain has a comma shape that lines up quite well with the inner negative potential island in Fig. 24a. The corresponding E_r plot in bulk plasma (cyan curve in Fig. 22) shows a change of sign around the $r = 0.8\,cm$ mark which matches with the radial position of the $v_{ir} = 0$ transition layer in Fig. 26a. Hence the different diagnostics results in Figs. 26a, 24a, and 22-cyan curve, are in good agreement.

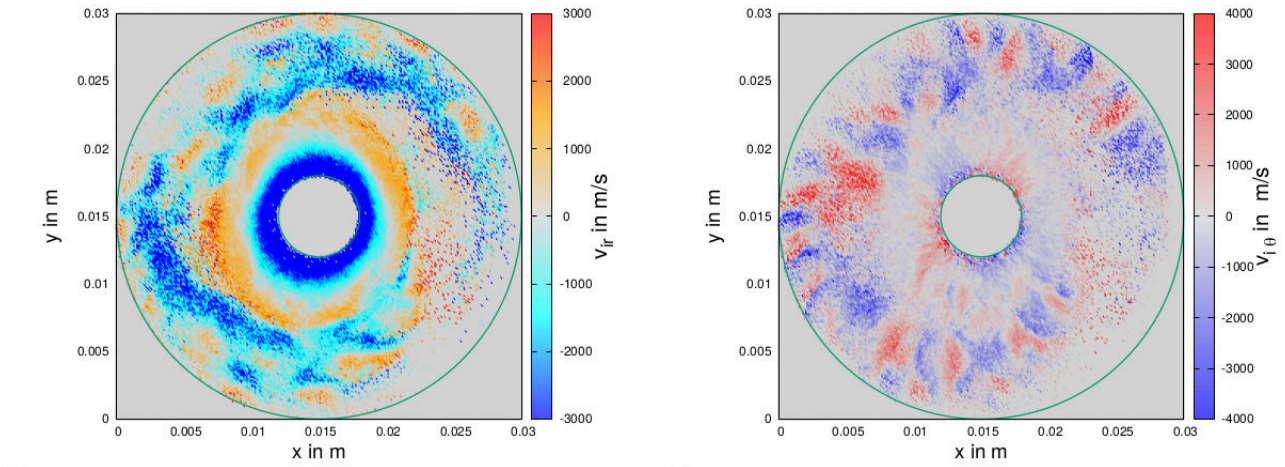

FIG. 18: [40 mTorr Ar-pressure] Ion velocity maps at $t = 0.665\,\mu s$ (nonlinear stage): (a) is map of the radial ion velocity v_{ir}, and (b) is a map of the azimuthal ion velocity $v_{i\theta}$

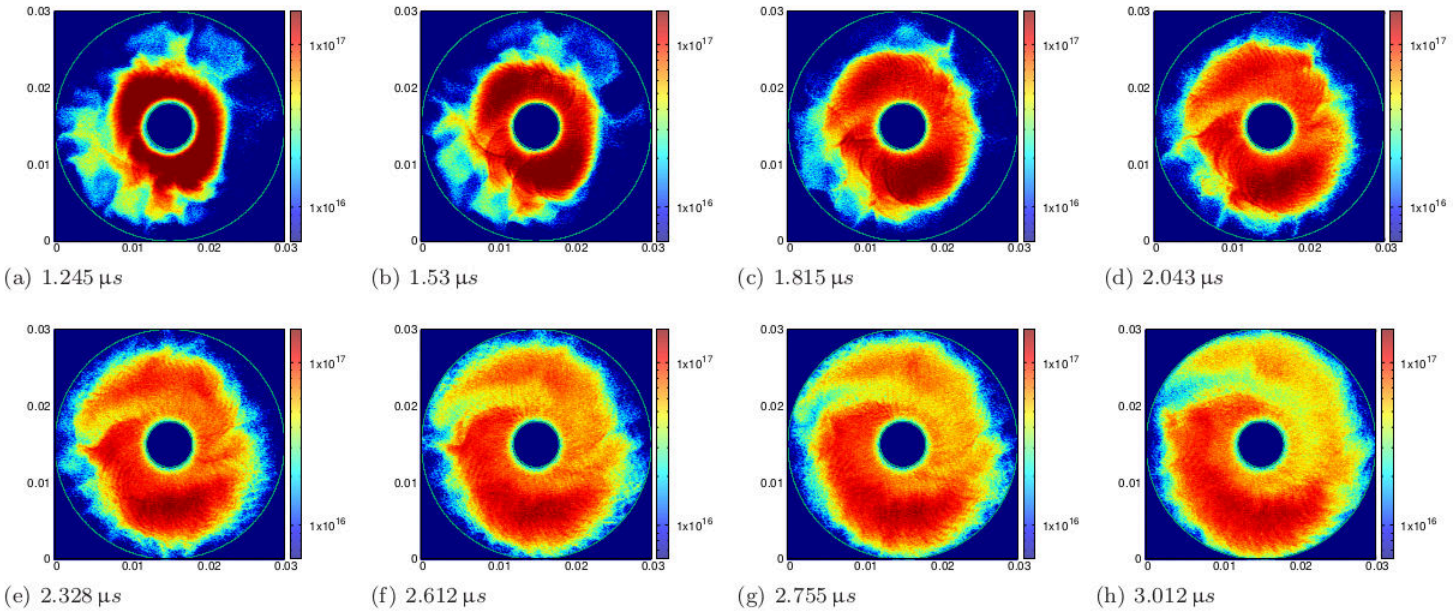

FIG. 19: Evolution of the ion density function after Ar-pressure reduction to $1\,mTorr$ at $t = 1.235\,\mu s$: (a)-(b) show short scale structures. In (c)-(d) the short structures have been engulfed by the expanding plasma. (e)-(h) show a nonlinear long spiral spoke.

Fig. 26b is a map of the ion azimuthal velocities at $t = 2.612\mu s$. Alternating red and blue structures indicate ion dragging by the E_θ. For instance, consider the filamental red patch extending North-West from the top of the cathode. This region corresponds to the double layer channel between the purple patch and the upper red patch in Fig. 24a. Local E_θ in this channel is essentially pointing downward i.e. anti-clockwise. This accounts for the positive $v_{i\theta}$ velocities in this strip.

V. INFLUENCE OF ELASTIC ELECTRON SCATTERING ON ROTATING SPOKES

We re-simulated the experiment of Sec III, this time with the non-ionizing elastic and excitation collisions between electrons and Ar-neutrals included in the MCC. By comparing the results from this simulation with those from Sec III, we were able to filter out the effects of Elastic Electron Scattering (EES) on the rotating spoke instability.

From a linear-theory standpoint, inclusion of an elastic

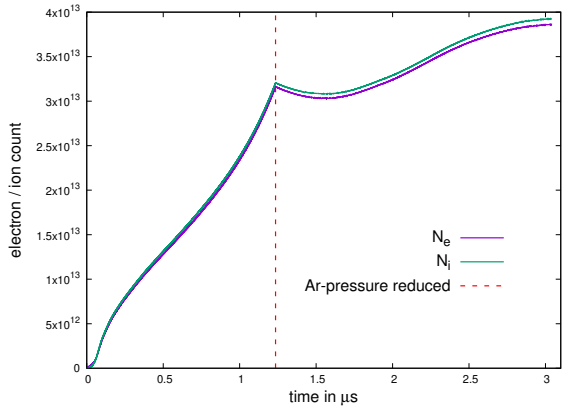

FIG. 20: The number of confined electrons N_e, and confined ions N_i in the device are plotted as function of time. The red dashed line represents $t = 1.235\,\mu s$, the point of Ar-pressure reduction.

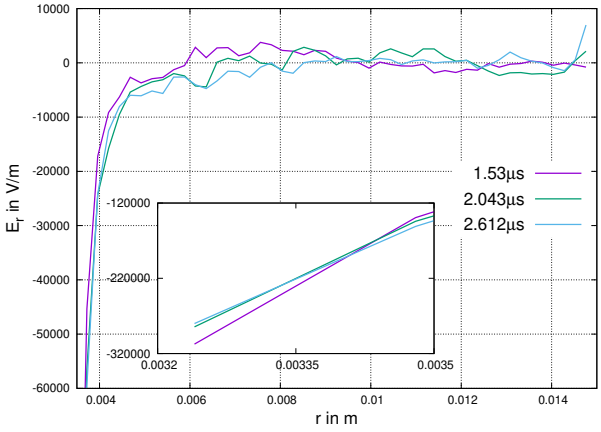

FIG. 22: [1mTorr Ar-pressure] Azimuthally averaged profiles of the radial electric field E_r are plotted between the walls at different stages of the instability. (Inset) The same profiles are zoomed-in on the cathode-sheath region

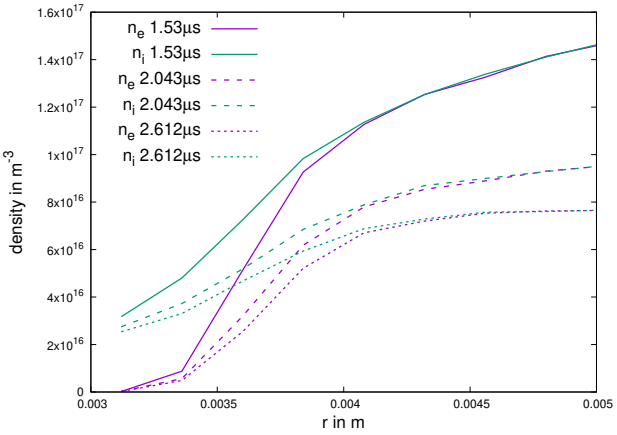

FIG. 21: [1mTorr Ar-pressure] The disintegration of the cathode sheath: The radial density profiles of ions, n_i and electrons, n_e in the near cathode region are plotted at different stages of disintegration of the ion sheath.

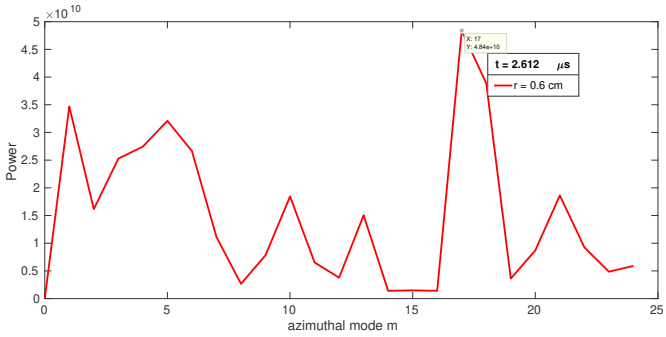

(a)

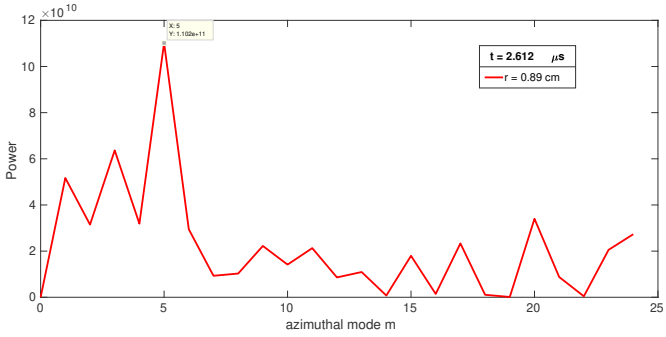

(b)

FIG. 23: [1 mTorr Ar-pressure]. FFT of the azimuthal electron density on radial surfaces, (a) $r = 0.6\,cm$ and (b) $r = 0.89\,cm$ at $t = 2.612\,\mu s$ (after Ar-pressure reduction)

collision frequency term in the lower hybrid dispersion (keeping other parameters unchanged) flattens the dispersion curve[49]. The maximum growth rate in the mode spectrum is lowered without any significant shift of the resonant mode number. However higher m modes to the right of the resonant mode now become accessible by the instability, as the inclusion of elastic collisions in the dispersion equation removes the upper cut-off boundary at the most resonant mode. So in effect, collisions makes the dispersion curve tend towards an ion-sound instability dispersion.

In experiments however, the role of EES can be more

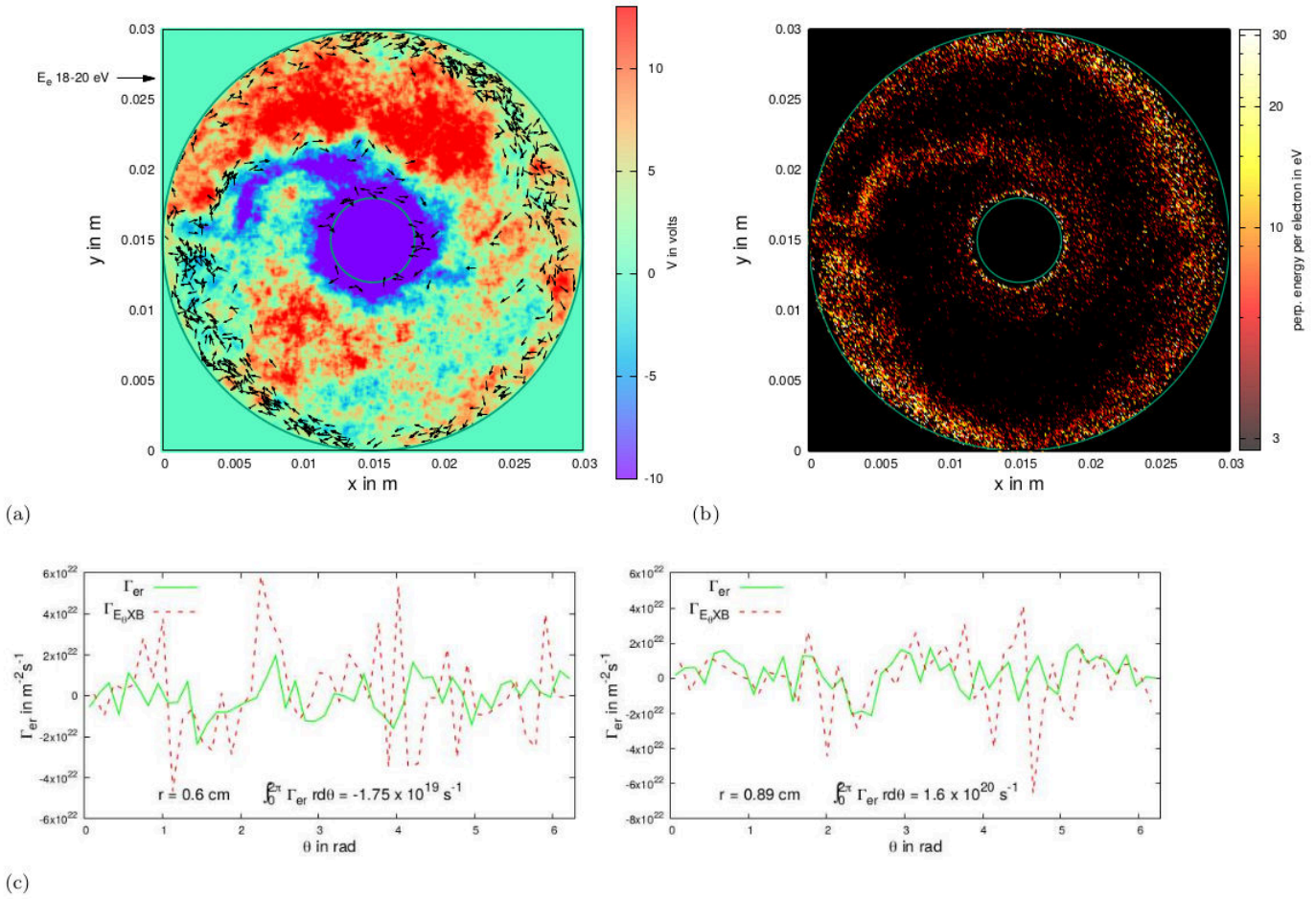

FIG. 24: [1 mTorr Ar-pressure] Electron dynamics after Ar-pressure reduction ($t = 2.612\,\mu s$): (a) is a colour contour of the potential V. A vector plot of electron flow in the 18-20 eV range (exact magnitudes undepicted) is superimposed. (c) The radial electron flux density , Γ_{er} is plotted on two radial surfaces, (left) $r = 0.6\,cm$, and (right) $r = 0.89\,cm$. The red dashed lines represent the calculated anomalous flux density $\Gamma_{E_\theta \times B}$ on the two surfaces. The total electron flux on the surfaces are also printed on the figures.

complex. For example, the cumulative effects of their small but finite kinetic energy dissipation directly affects the ionization rate of the discharge. The ionization rate in turn sets up the profiles density, density gradient, and electric field in the discharge that determine the outcome of the instability.

Fig. 27 shows the evolution of the ion density function in the presence of elastic, excitation, and ionizing collisions at 40mTorr Ar-pressure. Of the time-frames, Fig. 27a is in the linear growth stage, Fig. 27b is in the knee of the saturation, and Fig. 27e-h are in the saturated stage of the instability. Qualitatively the evolution is quite similar to Fig. 3 in Sec III. The instability starts off as long $m = 2$ structure as seen in Fig. 27b-c. With the diminishing of the E_r in bulk plasma, the mode transforms into the short scale structures visible in Fig 27d-h.

The transition of the electrostatic energy curve from linear growth to nonlinear saturation is shown in Fig. 28a. For comparison the corresponding curve of the EES-excluded simulation in Sec III is also plotted. In presence of EES the instability records a slightly lower linear growth rate, $\gamma = 2.6\omega_{lh}$ compared to $\gamma = 2.85\omega_{lh}$ when the EES are absent.

The influence of EES on the ionization dynamics is visualized in Fig. 28b which compares electron and ion populations curves between the EES and the No-EES simulations. In early stages of the discharge, elastic collisions enhance the ionization process which causes a faster growth of the EES-population curves at $t < 0.2\,\mu s$. The exact mechanism of this enhancement can not be ascertained. It could be possible that EES allows electrons to transit to higher energy orbits faster. In the long-run however, the cumulative energy dissipation from elastic collisions brings down electron energies by a significant amount to statistically impede the ionization process. At the end of the simulations at $t = 1.235\,\mu s$ the net population in the EES simulation is about an order of magnitude lower than that in the No-EES simulation.

As a supplement to the population curves the average

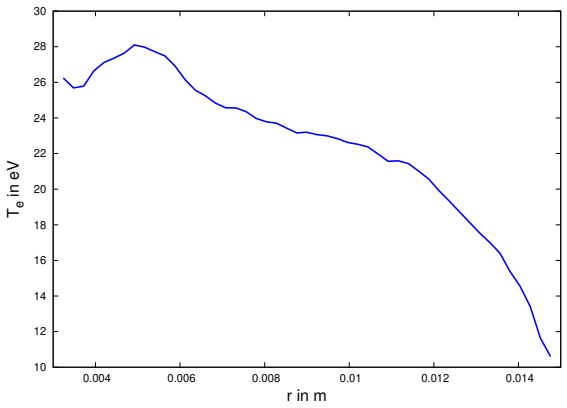

FIG. 25: [1 mTorr Ar-pressure] Radial profile of electron temperature, T_e at $t = 2.612\,\mu s$ (after Ar-pressure reduction).

3D kinetic energy per electron, $< K_e >$ in the two simulations are plotted as a functions of time in the inset of Fig. 28b. The average kinetic energies in both simulations show good correlation with corresponding population growths from ionization. At $t < 0.2\,\mu s$ the $< K_e >$ of the EES simulation is higher than that in the No-EES simulation. Thereafter the EES-$< K_e >$ curve falls below its No-EES counterpart. At $t = 1.235\,\mu s$ the $< K_e >$ values in the EES and No-EES simulation are 5eV and 6eV respectively.

Fig. 28c compares the radial flux density function between the EES and No-EES simulations at $t = 0.057\,\mu s$ (Fig. 3b and Fig. 27b) on the surface, $r = 0.6\,cm$. The corresponding $E_\theta \times B$ drift estimations of the flux densities are also plotted as dotted curves. The EES Γ_{er} displays a slightly weaker correlation with its drift estimate, especially in the azimuthal range $1 < \theta < 3.5$, which could possibly be the effect of collision driven radial electron transport in the EES simulation.

The 3D electron temperature profiles in the EES and the No-EES simulation at $t = 0.057\,\mu s$ are plotted in Fig. 28d. Overall, in the EES simulation temperatures are about 50% of that in the No-EES simulation. The thermal energies are lower in EES simulation because of collisional energy dissipation.

VI. CONVERGENCE TEST

Convergence tests are performed for the numerical experiment of Sec III by repeating the simulation with greater macro-particle representations. Two tests are performed; one with a macro-particle weight, $n_w = 7.565 \times 10^6$ that doubles particles-per-cell (ppc), and the other with $n_w = 4.450 \times 10^6$ that increases the ppc by a factor of 3.4. In a simulation with ionization, changing the macroparticle weight modifies the random number sequence used for particle generation. Hence effectively the convergence tests are performed on unidentical but equivalent kinetic ensembles of plasma.

Diagnostic results from the convergence tests are compared in Fig. 29. Fig. 29a is a tabular representation of the evolution of ion density in the original simulation versus the two tests. Note an angular phase difference in the excitation of the rotating spoke between the three simulations. The phase mismatch demonstrates that the orientation of the excited mode is random and not set by numerical factors like the rectangular mesh. The three simulations show similar propagation and wavelength modification of the rotating spokes with some differences in the details of the nonlinear shapes. The differences indicate some higher level sensitivities of the mode to the numerical representation of electron injection and ionization in the simulations.

Fig. 29b shows a convergent evolution of the net electrostatic energy in the three simulations. Fig. 29c compares the radial electron flux density on the $r = 0.6\,cm$ surface at $t = 0.057\,\mu s$ which also have an average agreement in magnitudes and level of fluctuations.

VII. CONCLUSIONS AND DISCUSSION

This work presents a numerical investigation of the rotating spoke structures in a partially magnetized ExB plasma of the cylindrical magnetron discharge. We have studied the spoke's nonlinear transitions which evolve self-consistently as a result of modifications in the radial electric field (due to the cathode sheath evolution) and changes in the neutral pressure of the system. Both these mechanisms of mode transition have been demonstrated and their effects on other dynamical aspects such as plasma heating and particle transport were studied.

In Sec III we studied the linear and nonlinear evolution of the rotating spoke at a fixed pressure of the background neutrals. The nascent discharge in the simulation is sparse and largely unshielded because of an unformed cathode sheath. The applied dc voltage drops across the entire radial profile, leading to a strong radial electric field in the quasineutral cloud. Penetrating electric field and collinear density gradient excite a lower hybrid instability that manifests as long wavelength ($m = 2$) rotating spoke. In the linear phase, the growth rate and rotation frequency of the spoke mode are both comparable to the characteristics of the lower hybrid eigen-mode in this plasma.

As more ions are created through electron impact ionization, an ion sheath develops around the cathode. Now the dc voltage is almost entirely dropped in the cathode sheath region, leaving significantly lower electric fields penetrating the quasi-neutral bulk and spoke. The shielding of the electric field reaching the spoke makes the long scale $m = 2$ mode unsustainable. The spoke undergoes wave-breaking forming short scale spoke-on-spoke

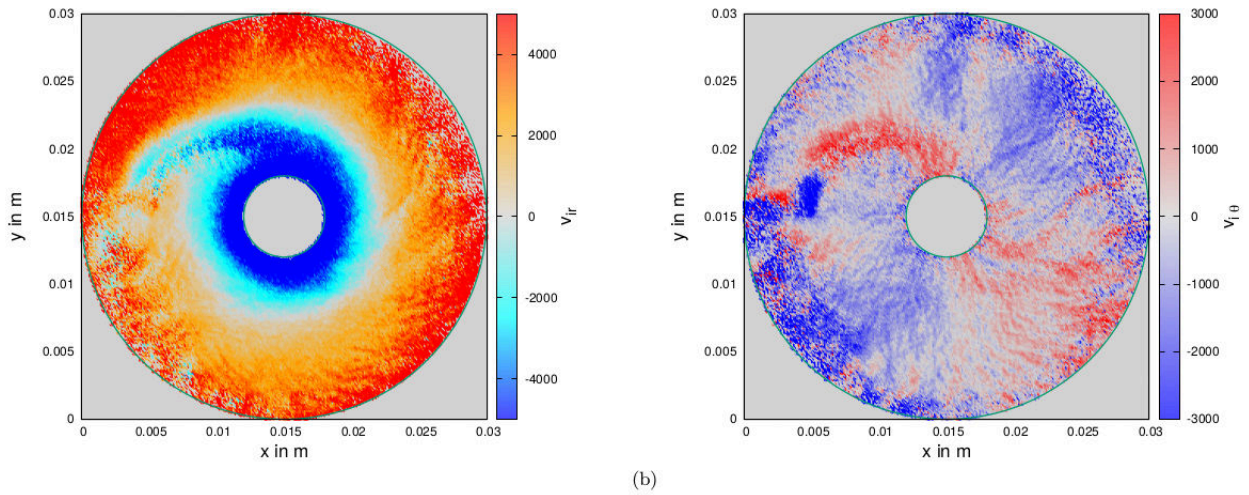

FIG. 26: [1 mTorr Ar-pressure] Ion velocity maps at $t = 2.612\,\mu s$ (after Ar-pressure reduction): (a) is map of the radial ion velocity v_{ir}, and (b) is a map of the azimuthal ion velocity $v_{i\theta}$

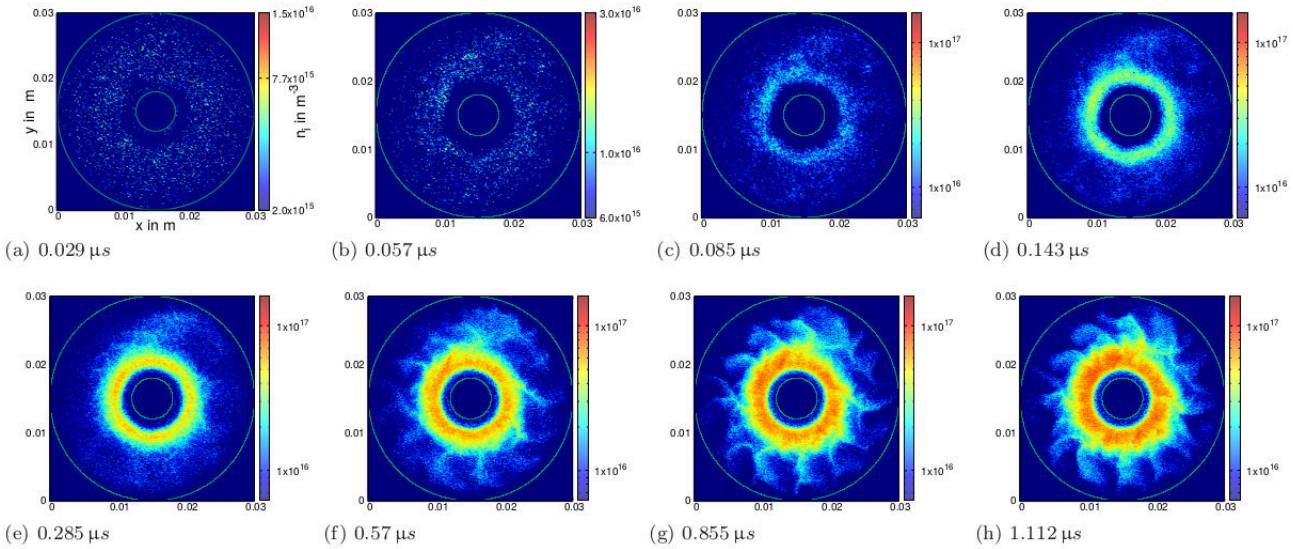

FIG. 27: Evolution of the ion density density at 40 $mTorr$ Ar-pressure in the presence of Elastic Electron Scattering (EES): (a)-(b) are in the linear phase and (c)-(h) are in the nonlinear phase of the plasma evolution.

modes. Eventually the long spoke collapses leaving only the short length structures.

It is interesting to note that this transition of the rotating spoke from a long mode to a short scale mode in the outer layers of the cloud, is modulated electrostatically by the cathode sheath dynamics happening deep inside the cloud.

In Sec IV we continued the simulation from where it was stopped in Sec III, only at a fraction (0.025) of the neutral pressure used in Sec III. Under reduced neutral fuel supply, the discharge expands radially into the void created by the uncompensated particle losses at the outer wall. The turbulent expansion stretches the cloud thin and also engulfs the short scale structures.

At the reduced plasma density the radial electric fields are revived which now excite a nonlinear long spiral spoke on the profile. The wavelengths of rotating spoke structures in planar magnetrons have been observed to scale similarly with neutral pressure[42]. We also find that the size of the rotating spoke and the plasma density inside the spoke are larger at the lower neutral pressure (compare Fig. 19e-h with Fig. 3e-h). Similar trends with changing argon pressure in the $mTorr$ range have been reported in the experiments of Ref. 29 and also observed in other ExB plasma devices such as Hall thrusters[74].

Spiral type structures are rather typical for some magnetron[39,41] and linear devices experiments[72,73]. The latter configurations is similar to what is considered in

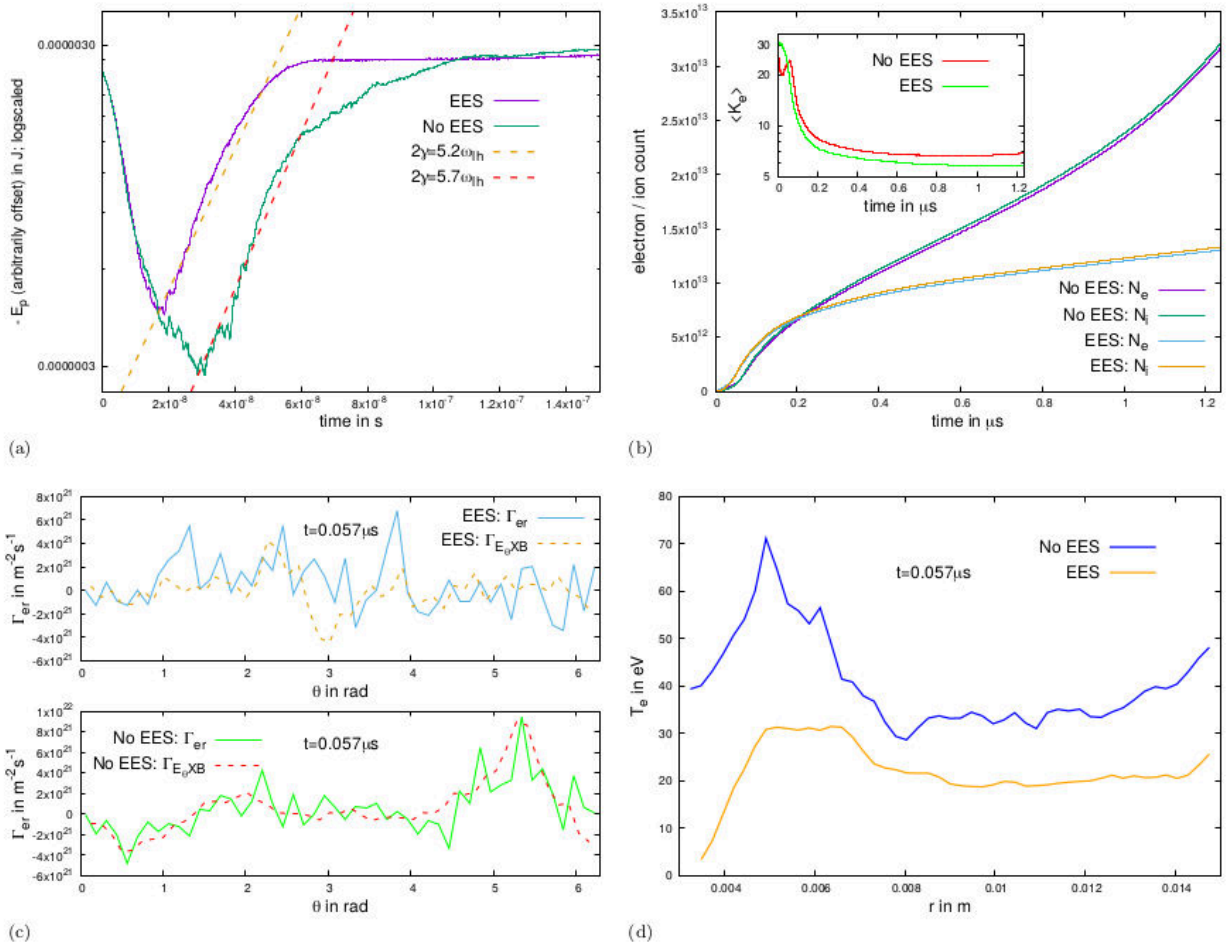

FIG. 28: [40 $mTorr$ Ar-pressure] A comparison of the instability evolution without EES and including EES using diagnostics *viz.* : (a) The electrostatic energy evolution and linear growth rate of the curve (b) The electron and ion population curves, (inset) the kinetic energy per electron $< K_e >$ vs time (c) the radial electron flux density on the surface $r = 0.6\,cm$ at $t = 0.057\,\mu s$ (d) The electron temperature as a function of radius at $t = 0.057\,\mu s$.

our paper. Similar structures have been also reproduced in fluid simulations of the gradient drift modes taking into account the dissipative effects[73]. It appears that the dissipation, which can be attributed to both elastic and non-elastic collisions, is an important factor that defines the characteristic spiral shape of the observed modes.

The radial electron flux densities on plasma surfaces were found to be in close agreement with corresponding $E_\theta \times B$ estimates throughout the simulation period in Sec III-IV. This confirmed that electrons were radially transported purely anomalously by azimuthal field structure attained in course of the mode transitions.

The azimuthal flow of the electrons begins as a rotating blob in the linear stage. When the long spoke arms starts breaking into short scale structures, the electron flow in the spoke has to loop around small equipotential islands that intersperse these short structures. The resulting electron vortices can even have opposing direction of the rotations to that of the underlying $E_r \times B$ flow. When the spiral long spoke comes into effect with the reduction of neutral pressure, the electron rotational flow gets constricted along narrow double layer channels which interlace large islands of equipotential.

Mapped distribution of azimuthal ion velocities across the simulation period, demonstrate that at all length scales of the spoke, ions get dragged by the azimuthal fields.

Radial ion velocity distributions also exhibit interesting wave-defined structures indicating that the spoke's field also has a radial component. A map of radial ion velocities in the turbulent phase following the drop in neutral pressure, shows the ion cloud getting separated into two transport domains - an inner domain of inward radial transport deep in the cathode's potential well, and an outer domain of outward transport driven by the plasma expansion.

Radial profiles of electron temperature plotted at different stages of the instability show that the cloud is relatively hotter whenever long scale structures are present because of heating by the associated large electric fields

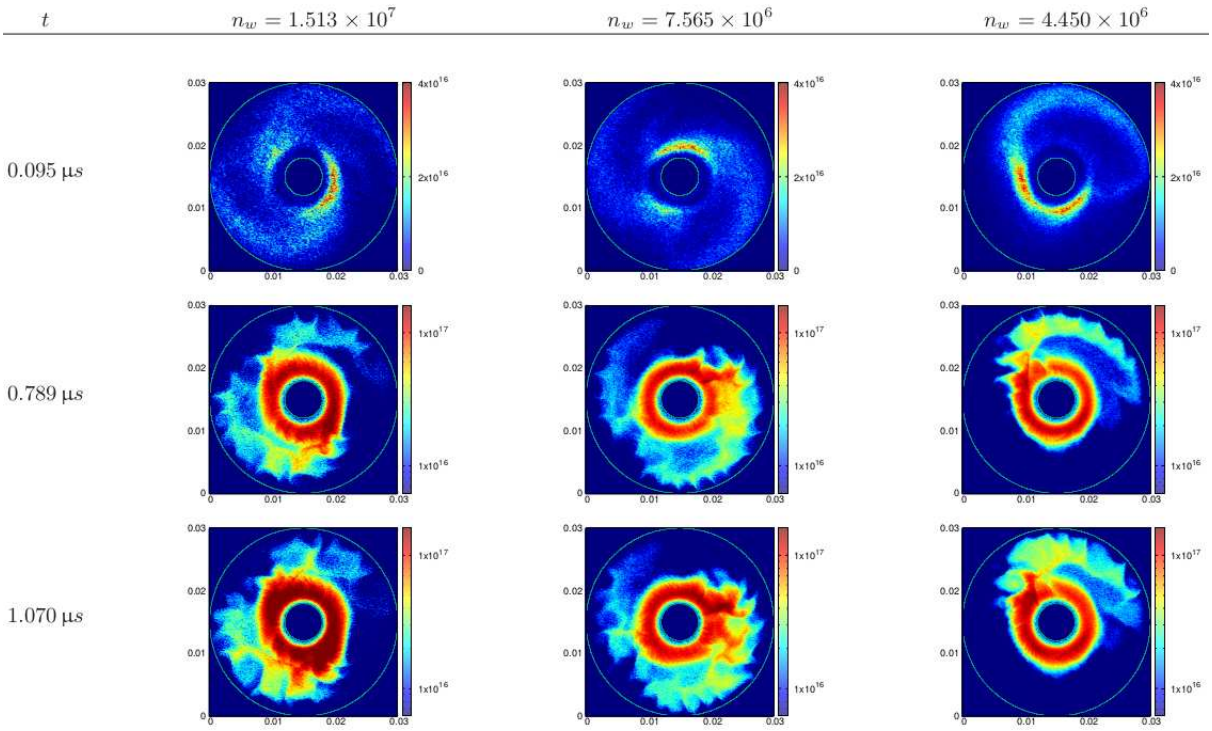

(a)

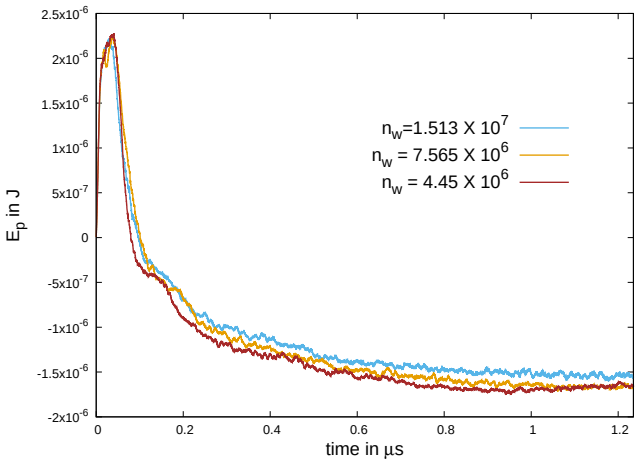

(b)

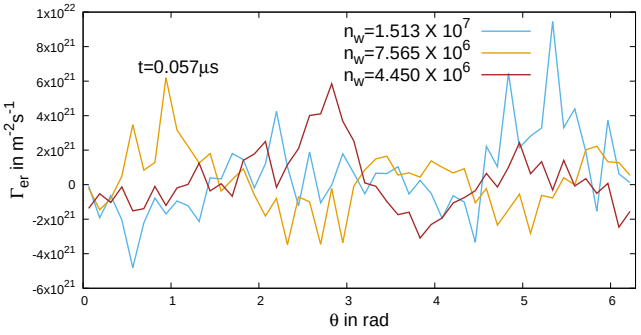

(c)

FIG. 29: Convergence test for the $40\,mTorr$-No EES simulation performed with macroparticle weights n_w values of 7.565×10^6 and 4.450×10^6 that correspond to a 2 times higher and 3.4 times higher particles-per-cell in simulation respectively : (a) compares the evolution of the 2D ion density function, (b) compares the evolution of the electrostatic energy, and (c) compares the radial electron flux density on the surface $r = 0.6\,cm$ at $t = 0.057\,\mu s$.

in the bulk plasma. In contrast, when the short scale structures are excited, the check on the E_r penetration by the cathode sheath, allows the cloud to cool to lower temperatures through transport of high energy particles.

Elastic electron scattering are not included in numerical experiment of Sec III-IV. Their effects are investigated in Sec V where the experiment of Sec III is repeated with the inclusion of EES in the collision model. The advanced collision model does not significantly alter the dynamics of mode transitions. However some effects are observed that can be attributed to the EES. These include a slightly slower linear growth of the lower hybrid instability, a reduction in ionization of the background neutrals owing to energy dissipation through EES, minor discrepancies between the $E_\theta \times B$ flux density profile and the measured radial electron flux density indicating minor collisional cross-field transport of the electrons, and overall lower electron temperatures again due to energy

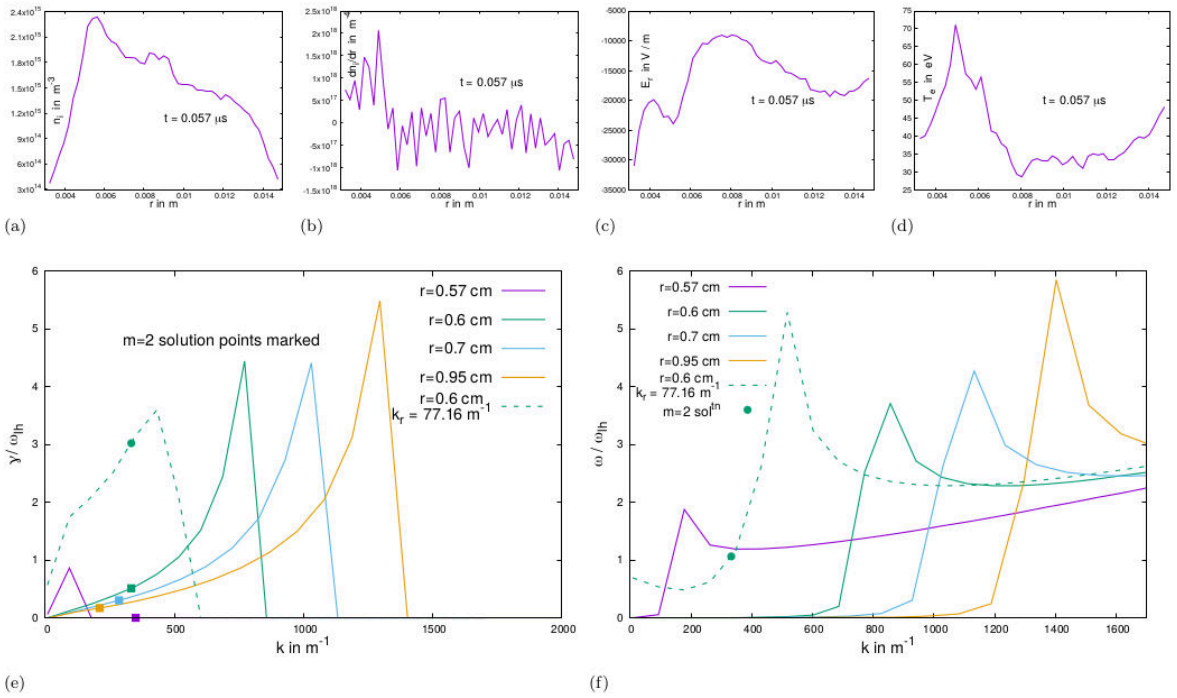

FIG. 30: Solutions of the linear lower hybrid instability dispersion on different radial surfaces at $t = 0.057\mu s$. (a)-(d) are radial profiles of the input plasma parameters *viz.*, (a) ion density, (b) radial ion density gradient, (c) radial electric field, and (d) electron temperature. (e) and (f) are dispersion solutions for the growth rate γ and frequency ω respectively plotted as functions of k, the azimuthal wave-vector. The green dashed dispersion curve represents the solution at $r = 0.6\,cm$ solved using a finite radial wave vector, $k_r = 77.16\,m^{-1}$. The point markers on the curves of (e)-(f) represent the solution for the $m = 2$ mode on that curve.

dissipation by EES.

Besides elastic collisions, enhanced localized ionization in the energetic double layers of the spoke is also expected to play a significant role in its nonlinear evolution[75–77]. In future works we aim to model the influence of ionization zones on the lower hybrid instability and vice versa[38,42,43].

In Sec VI a convergence test has been performed by re-simulating the experiment of Sec III with twice and 3.4 times the number of particles per cell. Diagnostic results from the tests such as the linear growth rate of the lower hybrid instability, the nonlinear structural transitions of the spoke, and the anomalous flux density of electrons on a radial surface, were found to be in very good agreement with the corresponding results from the original simulation. Hence the convergence test demonstrated the high fidelity of the PIC-MCC simulations using PEC2PIC.

ACKNOWLEDGMENTS

This work was carried out under grants from NSERC Canada and the U.S. Air Force Office of Scientific Research FA9550-15-1-0226 and FA9550-21-1-0031. Computational resources were provided by Compute Canada and the Plato cluster at the University of Saskatchewan.

DATA AVAILABILITY

The data that support the findings of this study are available from the corresponding author upon reasonable request.

Appendix: Insights on the growth of the m=2 spoke structure from the linear theory analysis

In the experiment of Sec III, the lower hybrid instability has an exponential (linear) growth phase manifested as a pure $m = 2$ mode. We have measured the linear mode's growth rate and frequency in simulations. Here we compare these results with the values from the linear theory. We show that while the local linear model does not yield a full quantitative match with the linear spoke excited in the inhomogeneous ExB discharge, it does reveals the parametric dependencies of the instability and provides good estimate for the experimental mode's frequency and growth rate.

In the absence of elastic collisions, the fluid linear dispersion for the lower hybrid instability takes the

form,[33,49]

$$\frac{\frac{kT_e\nabla_n}{Bn} + k^2\rho_e^2(\omega - \frac{kE}{B})}{(1+k^2\rho_e^2)(\omega - \frac{kE}{B})} = \frac{k^2c_s^2}{\omega^2}\,. \qquad \text{(A.1)}$$

Here ω and k represent the mode's complex frequency and its wave vector respectively. The E and B are the crossed electric and magnetic field and the k in this equation is assumed purely along the $E \times B$ direction, n and ∇n are the plasma density and density gradient, $\rho_e = (eT_e/m)^{1/2}/\omega_{ce}$ is the electron Larmor radius where e and m are the magnitudes of electron charge and the electron mass respectively, while $\omega_{ce} = eB/m$ is the electron cyclotron frequency. $c_s = (eT_e/M)^{1/2}$ is the ion sound speed, where M is the ion mass.

In our experiment, the plasma density gradient lengths scale and the radial electric field vary with radius. In general, a nonlocal analysis taking into account full radial inhomogeneities is required[78,79]. For large scale low m modes, it is expected that the global eigen-mode can be following some radially averaged profiles[26]. Therefore we solve the dispersion equation (A.1) on a set of radial surfaces of the discharge in the linear phase at $t = 0.057\mu s$ (Sec III, Fig. 3b). At this stage, Fig. 30a-d are the azimuthally averaged radial profiles of the input plasma parameters required to solve Eq. A1 viz., the ion density n_i ($\equiv n$), the ion-density gradient dn_i/dr ($\equiv \nabla n$), the radial electric field E_r ($\equiv E$), and the electron temperature T_e. Using Fig. 30a-d these parameters are extracted on the surfaces $r = 0.57, 0.6, 0.7, 0.95\,cm$. With these inputs, Eq. A1 is numerically solved on these 4 surfaces, to obtain the dispersion curves for the growth rate γ (Fig. 30e) and the frequency ω (Fig. 30f).

Although the theoretical dispersion curves in Fig. 30e-f are continuous, the experimental solution is actually discreet due to periodicity of the finite $2\pi r$ azimuthal domain. Only those k that give integer values of the azimuthal mode number, $m = kr$ are allowed. Further, owing to the cylindrical geometry, the k representing a particular mode numbers m, has a different value on each radial surface.

Fig. 30e shows the γ solutions in the normalized units of ω_{lh}. We label the $m = 2$ mode's solution on each surface with a square mark. The γ solutions for $m = 2$ all lie in the range 0 – $0.5\,\omega_{lh}$ which is lower than the experimental solution is $\gamma = 2.85\omega_{lh}$. The resonant k values in these solutions are also right-shifted towards wavelengths shorter than $m = 2$, with the exception of the $r = 0.57\,cm$ solution which has a left-shifted peak from $m = 2$.

Fig. 30f has the surface solutions for mode frequency expressed in units of ω_{lh}. To the left of the resonant k, frequency values remain close to zero. For the three solutions in the which the γ value peaks to the right of $m = 2$, the mode's frequency has negligibly small values, $\omega << \omega_{lh}$. The solution for the $r = 0.57\,cm$ dispersion has the $m = 2$ located within its resonant peak, hence produces a solution $\omega \sim \omega_{lh}$ which is agreeable with the measured frequency from simulation, $\omega = 1.023\omega_{lh}$.

In fact, the global solution has a finite radial extent which can be modeled by the finite value of the radial wave vector along E_r. Our simulation results also indicate that the rotating spoke is a 2D azimuthal-radial structure, e.g. the radial ion dragging map, Fig. 18a. When the radial wave vector is included, the dispersion equation gets modified as follows[49]

$$\frac{\frac{kT_e\nabla_n}{Bn} + \kappa^2\rho_e^2(\omega - \frac{kE}{B})}{(1+\kappa^2\rho_e^2)(\omega - \frac{kE}{B})} = \frac{\kappa^2c_s^2}{\omega^2}\,. \qquad \text{(A.2)}$$

In this equation k represents the wave vector component in the ExB direction, while κ represents the 2D wave vector so that $\kappa^2 = k^2 + k_r^2$, where k_r is the wave vector along E (here radial).

The introduction of a realistic k_r on the local dispersion equation gets the solutions more in sync with the simulation results. We tested with a $k_r = 77.16m^{-1}$ on the radial surface $r = 0.6\,cm$ (dashed line solutions in Fig. 30e-f) keeping all surface parameters unaltered. This k_r value is realistic as it represents a radial mode lengthscale of $0.8\Delta r$ where Δr is the separation between the inner and outer radial walls. Using this k_r in the Eq. A2, we get the solution $\gamma = 3.02\omega_{lh}$ and a $\omega = 1.062\omega_{lh}$ for the $m = 2$ mode. These values are in good agreement with the simulation results $\gamma = 2.85\omega_{lh}$ and $\omega = 1.023\omega_{lh}$. Further in this solution the $m = 2$ falls inside the resonant dome of the dispersion curve (Fig. 30e), and its γ is quite close to the peak value as well.

The effects of a finite k_r in the linear dispersion solution can be noted as - a) a left-shift of γ towards longer azimuthal wavelength, b) a reduction in the height of resonance peak and c) raising the frequencies of long wavelength modes making them comparable to ω_{lh}. As a result of these effects the local solutions become more agreeable with the simulation results.

Therefore we can conclude here that while Eqs. A1 and Eq. A2 do not provide linear global solution in the inhomogeneous plasma, inclusion of an appropriate k_r in the linear model shifts the analytical solutions closer to the experimental results. Despite the inhomegeneity of parameters of the plasma cloud, experimentally a linear pure $m = 2$ mode is realized on the profile indicating the global excitation.

[1] J.-P. Boeuf, J. Appl. Phys. **121**, 011101 (2017).
[2] M. Cappelli, Physics Today **62**, 76 (2009).
[3] C. L. Ellison, Y. Raitses, and N. J. Fisch, Phys. Plasmas **19**, 013503 (2012).
[4] S. N. Abolmasov, Plasma Sources Sci. Technol. **21**, 035006 (2012).
[5] J. P. Boeuf, J. Claustre, B. Chaudhury, and G. Fubiani, Phys. Plasmas **19**, 113510 (2012).
[6] I. D. Kaganovich, A. Smolyakov, Y. Raitses, E. Ahedo, I. G. Mikellides, B. Jorns, F. Taccogna, R. Gueroult, S. Tsikata, A. Bourdon, J.-P. Boeuf, M. Keidar, A. T. Powis, M. Merino, M. Cappelli, K. Hara, J. A. Carlsson, N. J. Fisch, P. Chabert, I. Schweigert, T. Lafleur, K. Matyash, A. V. Khrabrov, R. W. Boswell, and A. Fruchtman, Phys. Plasmas **27**, 120601 (2020).
[7] S. P. Gary and J. J. Sanderson, J. Plasma Phys. **4**, 739 (1970).
[8] D. W. Forslund, R. L. Morse, and C. W. Nielson, Phys. Rev. Lett. **25**, 1266 (1970).

[9]T. Lafleur, S. D. Baalrud, and P. Chabert, Phys. Plasmas **23**, 053502 (2016).
[10]T. Lafleur, S. D. Baalrud, and P. Chabert, Phys. Plasmas **23**, 053503 (2016).
[11]O. Buneman, J. Nucl. Energy, Part C Plasma Phys. **4**, 111 (1962).
[12]S. Janhunen, A. Smolyakov, D. Sydorenko, M. Jimenez, I. Kaganovich, and Y. Raitse, Phys. Plasmas **25**, 082308 (2018).
[13]J. C. Adam, A. Héron, and G. Laval, Phys. Plasmas **11**, 295 (2004).
[14]T. Lafleur and P. Chabert, Plasma Sources Sci. Technol. **27**, 015003 (2018).
[15]P. Coche and L. Garrigues, Phys. Plasmas **21**, 023503 (2014).
[16]V. Croes, T. Lafleur, Z. Bonaventura, A. Bourdon, and P. Chabert, Plasma Sources Sci. Technol. **26**, 034001 (2017).
[17]A. Héron and J. C. Adam, Phys. Plasmas **20**, 082313 (2013).
[18]F. Taccogna and P. Minelli, Phys. Plasmas **25**, 061208 (2018).
[19]K. Hara and S. Cho, "Radial-azimuthal particle-in-cell simulation of a Hall effect thruster," in 35th International Electric Propulsion Conference, Atlanta, GA, October (2017), IEPC Paper 2017-495.
[20]M. Lampe, J. B. McBride, W. Manheimer, R. N. Sudan, R. Shanny, J. H. Orens, and K. Papadopolous, Physics of Fluids **15**, 662 (1972).
[21]J. Cavalier, N. Lemoine, G. Bonhomme, S. Tsikata, C. Honoré, and D. Grésillon, Phys. Plasmas **20**, 082107 (2013).
[22]S. Janhunen, A. Smolyakov, O. Chapurin, D. Sydorenko, I. Kaganovich, and Y. Raitse, Phys. Plasmas **25**, 011608 (2018).
[23]O. Koshkarov and A. Smolyakov, Phys. Rev. Lett. **122**, 185001 (2019).
[24]M. J. Sekerak, A. D. Gallimore, D. L. Brown, R. R. Hofer, and J. E. Polk, Journal of Propulsion and Power **32**, 903 (2016).
[25]Z. A. Brown and B. A. Jorns, Phys. Plasmas **26**, 113504 (2019).
[26]M. Sengupta and A. Smolyakov, Phys. Plasmas **27**, 022309 (2020).
[27]A. Simon, Phys. Fluids **6**, 382 (1963).
[28]F. C. Hoh, Phys. Fluids **6**, 1154 (1963).
[29]Y. Sakawa, C. Joshi, P. K. Kaw, F. F. Chen, and V. K. Jain, Physics of Fluids B-Plasma Physics **5**, 1681 (1993).
[30]A. Ducrocq, J. C. Adam, A. Héron, and G. Laval, Phys. Plasmas **13**, 102111 (2006).
[31]T. Ito, C. V.Young, and M. A. Cappelli, Appl. Phys. Lett. **106**, 254104 (2015).
[32]J. B. Parker, Y. Raitses, and N. J. Fisch, Appl. Phys. Lett. **97**, 091501 (2010).
[33]J. P. Boeuf, Phys. Plasmas **26**, 072113 (2019).
[34]K. Matyash, R. Schneider, S. Mazouffre, S. Tsikata, and L. Grimaud, Plasma Sources Sci. Technol. **28**, 044002 (2019).
[35]N. Brenning, D. Lundin, T. Minea, C. Costin, and C.Vitelaru, J. Phys. D **46**, 084005 (2013).
[36]N. Brenning and D. Lundin, Phys. Plasmas **19**, 093505 (2012).
[37]J. P. Boeuf and M. Takahashi, PRL **124**, 185005 (2020).
[38]A. Anders, P. Ni, and A. Rauch, J. Appl. Phys. **111**, 053304 (2012).
[39]A. Hecimovic, V. S. von der Gathen, M. Böke, A. von Keudell, and J. Winter, Plasma Sources Sci. Technol. **24**, 045005 (2015).
[40]J. Held, P. Maaß, V. v.d. Gathen, and A. Keudell, Plasma Sources Sci. Technol. **29**, 025006 (2020).
[41]A. Hecimovic and A. von Keudell, J. Phys. D: Appl. Phys. **51**, 453001 (2018).
[42]M. Panjan, S. Loquai, J. Klemberg-Sapieha, and L. Martinu, Plasma Sources Sci. Technol. **24**, 065010 (2015).
[43]M. Panjan, J. Appl. Phys. **125**, 203303 (2019).
[44]J. Hnilica, P. Klein, M. Šlapanská, M. Fekete, and P. Vasina, J. Phys. D: Appl. Phys. **51**, 095204 (2018).
[45]A. T. Powis, J. A. Carlsson, I. D. Kaganovich, Y. Raitses, and A. Smolyakov, Phys. Plasmas **25**, 072110 (2018).
[46]E. Rodríguez, V. Skoutnev, Y. Raitses, A. Powis, I. Kaganovich, and A. Smolyakov, Phys. Plasmas **26**, 053503 (2019).
[47]J. Carlsson, I. Kaganovich, A. Powis, Y. Raitses, I. Romadanov, and A. Smolyakov, Phys. Plasmas **25**, 0612010 (2018).
[48]A. Hecimovic, C. Maszl, V. S. von der Gathen, M. Böke, and A. von Keudell, Plasma Sources Sci. Technol. **25**, 035001 (2016).
[49]A. I. Smolyakov, O. Chapurin, W. Frias, O. Koshkarov, I. Romadanov, T. Tang, M. Umansky, Y. Raitses, I. D. Kaganovich, and V. P. Lakhin, Plasma Phys. Control. Fusion **59**, 014041 (2017).
[50]W. Frias, A. I. Smolyakov, I. D. Kaganovich, and Y. Raitses, Phys. Plasmas **19**, 072112 (2012).
[51]R. Rane, M. Bandyopadhyay, M. Ranjan, and S. Mukherjee, Phys. Plasmas **23**, 013514 (2016).
[52]T. Richard, I. Furno, A. Sublet, and M. Taborelli, Plasma Sources Sci. Technol. **29**, 095003 (2020).
[53]M. Sengupta and R. Ganesh, Phys. Plasmas **21**, 022116 (2014).
[54]M. Sengupta and R. Ganesh, AIP Conf. Proc. **1668**, 020005 (2015).
[55]M. Sengupta and R. Ganesh, Phys. Plasmas **22**, 072112 (2015).
[56]M. Sengupta and R. Ganesh, Phys. Plasmas **23**, 102111 (2016).
[57]M. Sengupta and R. Ganesh, Phys. Plasmas **24**, 032105 (2017).
[58]M. Sengupta, "Studies in non-neutral plasmas using particle-in-cell simulations," PhD Thesis, HBNI, 2017.
[59]C. K. Birdsall and A. B. Langdon, *Plasma Pysics Via Computer Simulation* (Taylor and Francis Group, 2004).
[60]C. Zhang, H. Lan, Y. Ye, and B. D. Estrade, "Parallel SOR Iterative Algorithms and Performance Evaluation on a Linux Cluster," `http://www.ntis.gov/search/product.aspx?ABBR=ADA449212`, proceedings of the International Conference on Parallel and Distributed Processing Techniques and Applications, PDPTA 2005, Las Vegas, Nevada, USA, June 27-30, 2005, Vol 1.
[61]L. Olsen-Kettle, "Numerical Solution of partial differential equation," `http://espace.library.uq.edu.au/view/UQ:239427`, lecture notes at University of Queensland, Australia, 2011.
[62]S. A. Chin, Phys. Rev. E **77**, 066401 (2008).
[63]C. C. Lalescu, "Implementation of Splitting-Composition Schemes for the Numerical Study of Charged Particles," `http://www.researchgate.net/profile/Cristian_Lalescu/publications/?pubType=article` (2008).
[64]C. K. Birdsall, IEEE Transactions on Plasma Science **19, issue 2**, 65 (1991).
[65]V. Vahedi and M. Surendra, Computer Physics Communications **87**, 179 (1995).
[66]K. Nanbu and S. Uchida, Proc. 19th Int. Symp. Rarefied Gas Dynamics **1**, 601 (1994).
[67]K. Nanbu and S. Uchida, Jpn. J. Appl. Phys. **33**, 4752 (1994).
[68]M. Frignani and G. Grasso, "Argon cross sections for PIC-MCC codes," `http://www.afs.enea.it/ggrasso/files/reports/LIN-R01.2006.pdf` (2006).
[69]A. Okhrimovskyy, A. Bogaerts, and R. Gijbels, Phys. Rev. E **65**, 037402.
[70]M. Horký, W. J. Miloch, and V. A. Delong, Phys. Rev. E **95**, 043302 (2017).
[71]J.-P. Boeuf and B. Chaudhury, PRL **111**, 155005 (2013).
[72]D. Reiser, N. Ohno, H. Tanaka, and L. Vela, Physics of Plasmas **21**, 032302 (2014).
[73]C. Schroder, O. Grulke, T. Klinger, and V. Naulin, Physics of Plasmas **11**, 4249 (2004).
[74]Y. Raitses, I. Kaganovich, and A. Smolyakov, Joint Conference of 30th International Symposium on Space Technology and Science 34th International Electric Propulsion Conference and 6th Nano-satellite Symposium, Hyogo-Kobe, Japan July 4-10, IEPC-2015-307 ISTS-2015-b-307 (2015).
[75]M. Panjan and A. Anders, J. Appl. Phys. **121**, 063302 (2017).
[76]F. Estrin, S. Karkari, and J. Bradley, J. Phys. D: Appl. Phys. **50**, 295201 (2017).
[77]A. Anders, M. Panjan, R. Franz, J. Andersson, and P. Ni, Appl. Phys. Lett. **102**, 144103 (2013).
[78]R. C. Davidson and H. Uhm, Phys. Fluids **20**, 1938 (1977).
[79]D. A. Schecter, D. H. E. Dubin, A. C. Cass, C. F. Driscoll, I. M. Lansky, and T. M. O'Neil, Phys. Fluids **12**, 2397 (2000).